

Towards Efficient and Accurate Spiking Neural Networks via Adaptive Bit Allocation

Yao Xingting^{a,b,*}, Hu Qinghao^{a,*}, Zhou Fei^c, Liu Tielong^{a,b}, Li Gang^a, Wang Peisong^a and Cheng Jian^{a,b,**}

^aThe Key Laboratory of Cognition and Decision Intelligence for Complex Systems, Institute of Automation, Chinese Academy of Sciences, Zhongguancun East Road No.95, Beijing, 100190, China

^bSchool of Future Technology, University of Chinese Academy of Sciences, Huaibei Zhuang No.380, Beijing, 101408, China

^cChina Electric Power Research Institute Co., Ltd, Future Science Park Binhe Avenue No.18, Beijing, 102211, China

ARTICLE INFO

Keywords:

spiking neural networks
neuromorphic computing
efficient computing
bit allocation

ABSTRACT

Multi-bit spiking neural networks (SNNs) have recently become a heated research spot, pursuing energy-efficient and high-accurate AI. However, with more bits involved, the associated memory and computation demands escalate to the point where the performance improvements become disproportionate. Based on the insight that different layers demonstrate different importance and extra bits could be wasted and interfering, this paper presents an adaptive bit allocation strategy for direct-trained SNNs, achieving fine-grained layer-wise allocation of memory and computation resources. Thus, SNN's efficiency and accuracy can be improved. Specifically, we parametrize the temporal lengths and the bit widths of weights and spikes, and make them learnable and controllable through gradients. To address the challenges caused by changeable bit widths and temporal lengths, we propose the refined spiking neuron, which can handle different temporal lengths, enable the derivation of gradients for temporal lengths, and suit spike quantization better. In addition, we theoretically formulate the step-size mismatch problem of learnable bit widths, which may incur severe quantization errors to SNN, and accordingly propose the step-size renewal mechanism to alleviate this issue. Experiments on various datasets, including the static CIFAR and ImageNet datasets and the dynamic CIFAR-DVS, DVS-GESTURE, and SHD datasets, demonstrate that our methods can reduce the overall memory and computation cost while achieving higher accuracy. Particularly, our SEWRNet-34 can achieve a 2.69% accuracy gain and 4.16× lower bit budgets over the advanced baseline work on ImageNet. This work will be open-sourced.

1. Introduction

Spiking neural networks (SNNs) are considered the third generation of neural networks due to their emulation of the human brain's information-processing mechanism [33]. The essential uniqueness of SNN is its activation unit, i.e., spiking neuron, which transfers floating-point values into binary spikes, thus making the matrix operations, e.g., convolution, conducted multiplication-free [15]. Similar to binary neural networks (BNN), binary feature maps (spikes) would reduce spatial representation capacity, making processing information-dense data challenging and resulting in lower model accuracy [57, 35, 56].

In this context, multi-bit spiking neural networks have recently arisen as a promising approach to improving such inadequate informational scope [18, 49, 50, 48]. As the name suggests, multi-bit SNNs introduce more bits to represent the original binary spike and devote more addition operations to process the matrix multiplication. Prior arts successfully incorporated this mechanism to improve accuracy, while

most neglected the actual memory and computation overhead as pointed out by [39]. For instance, a layer with less representation ability but assigned with higher bit widths would incur memory and computation waste and interfere with the model inference [12, 6]. It necessarily comes to the question: *Can we enhance SNN's performance while keeping memory and computation costs at minimal levels?*

In this paper, we investigate the adaptive bit allocation of quantized SNNs as the answer. Specifically, we parametrize the three fundamental elements of memory and computation: temporal lengths, bit widths of weights, and bit widths of spikes, making them learnable and able to be optimized end-to-end. To regulate the allocation process of temporal lengths and bit widths during training and ensure they converge to the targets correctly, we explicitly set temporal length and bit width bounds and implicitly design the regulating loss. By implementing these strategies, we can effectively assign different temporal lengths and bit widths to different layers, enabling a fine-grained allocation of memory and computation resources for SNN. Thus, the accuracy and efficiency of the inference can be improved. Moreover, unlike the memory and computation measurement of most prior arts [56, 18, 50, 52], we incorporate the pragmatic concept "Bit Budget" and the associated S-ACE, which are proposed by [39], to estimate the accurate model memory and computation overheads.

*Equal contribution

**Corresponding author

✉ yaoxingting2020@ia.ac.cn (Y. Xingting); huqinghao2014@ia.ac.cn (H. Qinghao); 1242643224@qq.com (Z. Fei); liutielong2022@ia.ac.cn (L. Tielong); gang.li@ia.ac.cn (L. Gang); wangpeisong2013@ia.ac.cn (W. Peisong); jian.cheng@ia.ac.cn (C. Jian)

ORCID(s): 0009-0000-1872-1170 (Y. Xingting); 0000-0003-0422-5509 (H. Qinghao); 0009-0006-8357-860X (Z. Fei); 0000-0001-7835-4739 (L. Gang); 0000-0003-1289-2758 (C. Jian)

Bit-adaptive Spiking Neural Networks

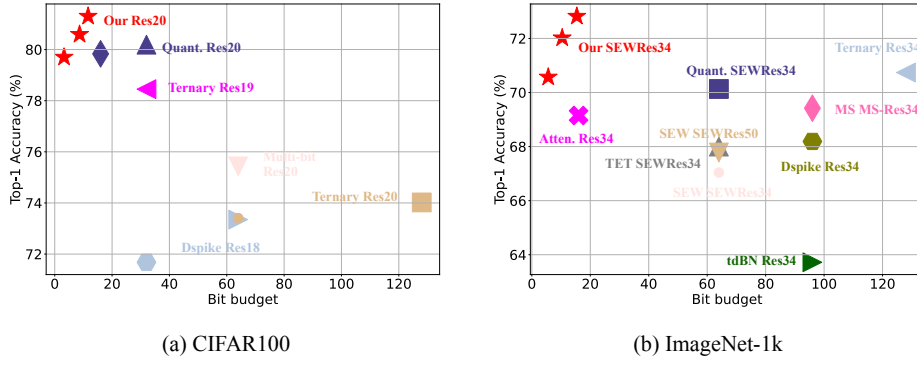


Figure 1: Comparisons with other advanced direct-trained SNNs using ResNet-based architectures on CIFAR100 and ImageNet-1k. Our models maintain the same level of model size as our baselines.

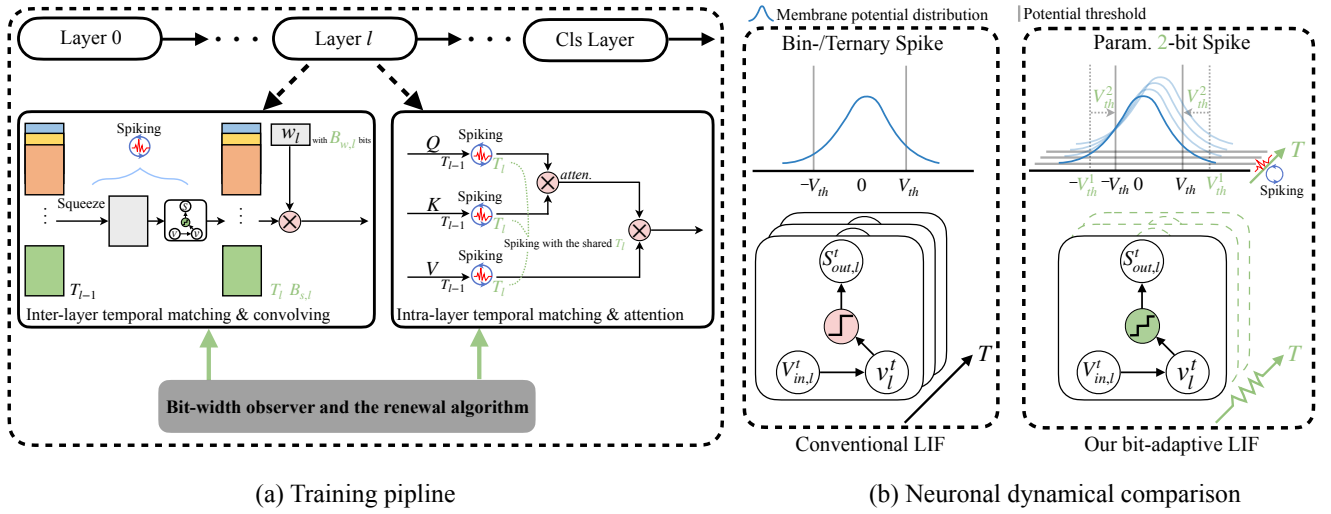


Figure 2: Overview of the proposed bit allocation method. Green notations denote the parametrized constants. **(a)** Adaptive-bit-allocation training pipeline, where the bit widths T_l , $B_{s,l}$, and $B_{w,l}$ are made learnable and adaptive. T_l is matched inter-layer and intra-layer to ensure fluent dataflow. The step-size renewal mechanism is also proposed to alleviate the step-size mismatch issue. **(b)** depicts the neuron formulation (bottom) and the potential division (top) of the previous spiking neuron (left) and our bit-adaptive spiking neuron (right). The temporal length T_l is layer-wise learnable and a shift $V_{th,l}^2$ is added to the potential threshold $V_{th,l}^1$.

With the above quantization and parametrization methods applied, new challenges concerning the unique temporal dimension of SNNs arise. Firstly, the length of the temporal dimension is a hyperparameter and initially does not get involved in the forward pass, thus failing to get gradients for optimization. Secondly, previous multi-bit spiking neurons are designed and tuned in a relatively arbitrary and empirical manner, showing less friendliness to quantization. Thirdly, the potential step-size mismatch issue of learnable bit widths may become more severe. Because once a wrong step size is applied, it will be consecutively used along the temporal dimension. As illustrated in Figure 2, we first refine the spiking neuron, which addresses inter-layer and intra-layer temporal mismatches arising from variable temporal lengths while minimizing quantization errors through improved formulations and potential division operations. Then, we formulate the quantization step-size mismatch issue, where

SNN would suffer statistically more quantization errors that accumulate along the temporal dimension. Accordingly, we propose the step-size renewal mechanism, which consists of a bit-width observer and the renewal algorithm as depicted in Figure 2. When the step-size mismatch is observed, the renewal algorithm will be triggered to rectify step sizes automatically, ensuring a better training forward pass.

For the proposed theory and techniques, we conduct extensive experiments to validate the effectiveness. In comparison with prior arts, we demonstrate that our approaches can achieve superior accuracy while maintaining lower bit budgets, as shown in Figure 1.

In summary, our contributions are as follows:

- We propose an adaptive bit allocation method to build high-performance SNNs with low bit budgets. To the best of our knowledge, this is the first work to

realize an adaptive bit allocation for SNNs with direct training.

- We accordingly refine the spiking neuron to exploit parametrization and temporal information, and achieve better experimental results during the adaptive bit allocation.
- We theoretically formulate the step-size mismatch issue that could severely harm the training of SNNs, and propose the step-size renewal mechanism to alleviate this issue, thus improving the overall model performance.
- We conduct thorough experimentation to demonstrate our proposed method’s effectiveness on both static and dynamic datasets. Comparative experiments also show that our model can achieve the advanced accuracy with lower bit budgets, as shown in Figure 1.

2. Related work

2.1. Supervised direct learning of SNNs.

Based on the idea that SNNs could be optimized end-to-end through back-propagation [37], Bothe et al. [5] first used the surrogate gradient (SG) to solve the non-differentiability of SNNs. Wu et al. [45] further compared and analyzed the impacts of the shapes of SG functions on model performance. Afterward, many practical techniques and architectural designs were developed to strengthen the direct-trained SNN performance, such as tdbn [55], SEW block [15], spiking self-attention (SSA) block [56], TET [11], etc. In this paper, we adopt the two main-stream direct-trained SEW and SSA to estimate the effectiveness of our proposed methods.

2.2. Multi-bit spiking neural networks.

Wu et al. [47] were the first to replace binary spikes with full-precision analog spikes to improve the model accuracy. Guo et al. added the spike amplitude coefficient [19] and negative spike [18] to realize ternary (2-bit) spikes. You et al. [50] and Xing et al. [50] concurrently introduced ternary spikes into natural language processing (NLP), and both achieved tremendous success. SpikeLLM [49] and Multi-bit SNN [48] were more aggressive. They extended ternary spikes to multiple bits (over 2 bits) to boost the SNN performance while theoretically proving that the characteristic of addition-only computation can still be maintained. Shen et al. [39] combined multi-bit SNNs with quantization and presented a rational and practical approach called "Bit Budget" to estimating computing overheads. Different from the above multi-bit SNNs, our work focuses on fine-grained bit allocations, with which multi-bit SNNs can substantially minimize the memory and computation and maximize the model accuracy.

2.3. Mixed-precision quantization.

Mixed-precision quantization is based on the insight that different layers in artificial neural networks (ANN) require

different degrees of representation ability. Wang et al. [43] and Wu et al. [44] were the pioneers that fostered the search-based means to allocate different bit widths with reinforcement learning and differentiable neural architecture search, respectively. While, Dong et al. [12] used Hessian metrics to represent the layer importance and accordingly assigned bit widths. Recently, optimization-based mixed-precision was developed to learn the bit width during training [42, 54, 24, 25]. Compared with the above methods, which focus solely on ANN mixed-precision, our work is among the first to target SNNs, addressing the additional temporal dimension and mitigating step-size mismatch.

3. Preliminaries

3.1. Multi-bit spiking neuron

Here, we begin by formulating the conventional Leaky Integrate-and-Fire (LIF) model in its discrete form:

$$v_l^t = \begin{cases} \frac{1}{\tau} v_l^{t-1} + V_{in,l}^t, & S_{out,l}^{t-1} = 0 \\ v_{rst}, & \text{otherwise} \end{cases} \quad (1)$$

$$S_{out,l}^t = \begin{cases} 1, & v_l^t > V_{th} \\ 0, & \text{otherwise} \end{cases} \quad (2)$$

where v_l^t denotes the membrane potential at time-step t in the layer l and can be updated with Equation 1. v_{rst} and τ , respectively representing the resting potential and the time coefficient, are constants. $V_{in,l}^t$, representing the input current, is a variable. In Equation 2, $S_{out,l}^t$ is the binary spike whose value is determined by whether the membrane potential v_l^t exceeds the membrane-potential threshold V_{th} . If that happened, v_l^t would be reset to v_{rst} . Plus, the input current $V_{in,l}^t$ is calculated from the previous layer’s $S_{out,l-1}^t$ via $V_{in,l}^t = \sum_j w_{l-1} S_{out,l-1}^t$, where w_{l-1} denotes the weight parameters and j denotes the index of spiking neurons.

Rooted from burst encoding [30], the multi-bit spiking neuron generalizes Equation 2 to allow multiple spikes at the same time-step. The formulation transforms into [39, 48, 49]:

$$V_{in,l}^t = \sum_j (w_{l-1} \cdot \alpha) S_{out,l-1}^t, \quad (3)$$

$$v_l^t = \frac{1}{\tau} v_l^{t-1} + V_{in,l}^t - \alpha \cdot S_{out,l}^{t-1}, \quad (4)$$

$$S_{out,l}^t = \left\lfloor \frac{v_l^t}{V_{th}} \right\rfloor. \quad (5)$$

Here, $\lfloor x \rfloor$ is the flooring function, and α is the spike amplitude coefficient. With such transformation, the representation space of the spiking neuron is increased to $S_{out}^t \in \{0, 1, \dots, 2^{B_s} - 1\}^T$. B_s and T denote the spike bit width and the temporal length, respectively.

3.2. Quantization of weight parameters.

For further improvement of SNN’s efficiency, prior work has employed weight quantization to compress the model

size, e.g., [39]. A classic quantization formula is given below:

$$w_q^l = \text{clip}\left(\frac{w_l}{S_q^l}\right), -2^{B_w-1} + 1, 2^{B_w-1} - 1) \cdot S_q^l, \quad (6)$$

where $\lfloor x \rfloor$ is the rounding function, S_q^l represents the quantization step size of layer l , B_w denotes the weight bit width, w_l is the weight parameter, and w_q^l is the quantized weight value. If $B_w = 1$, Equation 6 will switch to $w_q^l = \text{sign}(w_l/S_q^l) \cdot S_q^l$.

3.3. Legitimate computation and memory measurement.

Shen et al. [39] propose the "Bit Budget" paradigm to fairly and practically estimate the substantial computation and memory. Following is the definition:

$$\text{Bit budget (BB)} = T \cdot B_w \cdot B_s. \quad (7)$$

The corresponding computational expenses evaluation, named Arithmetic Computation Effort (S-ACE), is defined by:

$$\text{S-ACE} = \sum_{w \in W, s \in S} n_{w,s} \cdot \text{BB}. \quad (8)$$

$n_{w,s}$ is multiply-accumulate operations' number (MACs), W and S are weights and spikes' sets, respectively.

To measure the computational consumption of fully ideal neuromorphic hardware. Shen et al. [39] also propose the NS-ACE metric, which is calculated by:

$$\begin{aligned} \text{NS-ACE} &= \sum_{w \in W, s \in S} f r_s \cdot n_{w,s} \cdot \text{BB} \\ &\approx \bar{f} r_s \cdot \sum_{w \in W, s \in S} n_{w,s} \cdot \text{BB} \\ &= \bar{f} r_s \cdot \text{S-ACE}. \end{aligned} \quad (9)$$

Here, $f r_s$ ($\bar{f} r_s$) is the (average) firing rate of neurons, which is always less than 1.

Notably, we regard the temporal length T as a special "bit-width" since we have employed the concept of "Bit Budget". For conciseness, we will not explicitly distinguish between T and other bit widths (B_s, B_w) in the subsequent context.

4. Methodology

We build efficient and accurate SNNs by (1) quantizing SNNs, parametrizing bit widths, and refining the multi-bit spiking neuron formulation out of SNN's special necessity and better empiricism; (2) solving every non-differentiable term and designing the loss function to achieve learnable and controllable bit allocation; (3) formulating the step-size mismatch issue and alleviating it via the proposed step-size renewal.

4.1. Parametrization

We can observe that Equation 5 is essentially a flooring quantization process of v_l^t , where $S_{out,l}^t$ is the quantized integer, V_{th} is the quantization step size, and the quantized spike value is $\alpha \cdot S_{out}^t$. Therefore, SNN's feature map size is controlled by B_s and T . Similarly, the weight parameter size can also be controlled by the weight bit width B_w in Equation 6. Thus, the whole model's computation and memory overhead is controlled by B_s , T , and B_w , which is why the "Bit budget" metric [39] is valid and matters. However, previous SNN quantization [39] did not take into account a fine-grained allocation mechanism for these pivotal elements (B_s , T , and B_w), leading to suboptimal model efficiency.

Based on the insight that a layer with less representation ability but assigned with higher bit widths would incur memory and computation waste and interfere with the model inference [43, 6], we propose to parametrize the three pivotal elements layer-wise, making them learnable and can be optimized through back-propagation. Thus, a fine-grained allocation strategy would be feasible. Following are the parametrization formulas, including:

$$B_{s,l} = \lfloor \text{clip}(\hat{B}_{s,l}, 1, B_{s,bound}) \rfloor, \quad (10)$$

where $B_{s,bound}$ is the integer upper bound, which is manually set, $B_{s,l}$ is the spike bit width of layer l , and $\hat{B}_{s,l}$ is the learnable parameter of $B_{s,l}$. Similarly, the parametrization of T and B_w can be obtained:

$$T_l = \lfloor \text{clip}(\hat{T}_l, 1, T_{bound}) \rfloor, \quad (11)$$

$$B_{w,l} = \lfloor \text{clip}(\hat{B}_{w,l}, 1, B_{w,bound}) \rfloor. \quad (12)$$

As for the membrane-potential threshold V_{th} and the weight quantization step size S_q^l , no specific parametrization formulas are introduced since they inherently exist as floating-point values.

Consequently, different layers can attain suitable bit widths and temporal lengths for different data, leading to adaptive and flexible allocation of memory and computation.

4.2. Formulation of the refined parametric spiking neuron

With the quantization and parametrization implemented, the original multi-bit spiking neuron is unsuitable for the following bit-width learning process. Therefore, we refine its formulation out of necessity and empiricism.

Firstly, since the temporal length is made parametric and can be different among different layers during training, two issues arise: (1) the gradient requirement, i.e., T_l needs to get involved in the forward pass; (2) the temporal mismatch between layers. For example, the previous layer yields a spike train with $T = 2$, while the post layer has four temporal bits, i.e., $T = 4$. Two time-steps of data remain unfilled. To solve these issues, we exploit the temporal flexibility [51], directly squeezing the spike train through an averaging operation, as shown in Figure 2(a) and Equation 13. Notably, the extra computation brought by such temporal squeezing

is negligible because it only makes up less than 0.1% of the total model computation. In addition, the spiking self-attention[56] layer requires the three spike feature maps (Q , K , and V) to perform matrix multiplication, necessitating compatible feature map dimensions. Therefore, we enforce shared T_l among the corresponding spiking neurons to ensure the intra-layer temporal matching, as shown in Figure 2(a).

Secondly, the flooring operation in Equation 5 may induce extra quantization error that incurs model degradation. From a value quantization perspective, compared to the rounding operation, the flooring operation brings in more quantization errors, which is evident. The proof is given in the appendix. Therefore, we offer another choice: a membrane-potential shift can be added to the flooring operation of Equation 5, making Equation 5 equivalent to the rounding operation when the shift value is proper. Meanwhile, the original spike-fire format has also been maintained. The transformed Equation 5 is Equation 15. For the same reason, we find the time constant τ , apart from increasing stochasticity, is implausible. Therefore, setting $\tau = 1$ should also be considered. Based on the above insights, we conduct experiments in Table 4 as empirical support.

Thirdly, the spike amplitude coefficient α is usually defined differently among prior arts [39, 18, 48]. Here, we keep consistent with quantization’s perspective, and directly unify V_{th} and α as identical, layer-wise, learnable quantization step size, as shown in Equations 13- 15.

Eventually, we formulate our refined multi-bit spiking neuron in the following and illustrate it in Figure 2.

$$V_{in,l}^t = \sum_j w_q^{j-1} \cdot V_{th,l-1}^1 \cdot \frac{1}{T_{l-1}} \sum_{\tau} S_{out,l-1}^{\tau}, \quad (13)$$

$$v_l^t = \frac{1}{\tau} v_l^{t-1} + V_{in,l}^t - S_{out,l}^{t-1} V_{th,l}^1, \quad (14)$$

$$S_{out,l}^t = clip\left(\frac{v_l^t}{V_{th,l}^1} + V_{th,l}^{2,t}\right), 0, 2^{B_{s,l}^t} - 1), \quad (15)$$

where, in our practice, τ is suggested to be 1, the spike amplitude coefficient α is replaced by the learnable membrane-potential threshold $V_{th,l}^1$, and threshold shift $V_{th,l}^{2,t}$ equates to $0.5sign(v_l^t/V_{th,l}^1)$. Beyond this, to further increase the adaptivity [53, 50], we apply the temporal-wise sharing technique to $V_{th,l}^1$ and $B_{s,l}$. Following [53] and [50], we make $V_{th,l}^1$ and $B_{s,l}$ shared temporally along the temporal dimension, as shown in Equation 15. Specifically, $V_{th,l}^1 \Rightarrow V_{th,l}^{1,t} \in \{V_{th,l}^{1,1}, \dots, V_{th,l}^{1,t}, \dots, V_{th,l}^{1,T_{bound}}\}$. Similarly, $B_{s,l} \Rightarrow B_{s,l}^t \in \{B_{s,l}^1, \dots, B_{s,l}^t, \dots, B_{s,l}^{T_{bound}}\}$.

As suggested in [19, 18, 32], negative spikes should be enabled to improve the representation ability of SNNs. Therefore, we expand Equation 15 to the bidirectional domain, thus supporting negative spikes. Equation 15 would

turn into:

$$S_{out,l}^t = clip\left(\frac{v_l^t}{V_{th,l}^1} + V_{th,l}^{2,t}\right), -2^{B_{s,l}^t-1} + 1, 2^{B_{s,l}^t-1} - 1). \quad (16)$$

Notably, in our practice, we find that for both spiking ResNet and Spikformer, only the very first convolution layer would require such bidirectional spiking neuron to encode the RGB image signals or the bipolar event signals. At the same time, other layers keep using the positive multi-bit spiking neuron. As a result, models would achieve higher accuracy.

4.3. Adaptive bit width

With parametrized bit widths $B_{s,l}$, $B_{w,l}$ and T_l , and learnable quantization step sizes $V_{th,l}^1$, S_q^l as illustrated in the above subsections, this subsection further solves the non-differentiable terms appearing in the parametrization process and introduces the regulating loss, which regulates bit widths to converge to the targets during training.

4.3.1. Gradient calculations

We solve non-differentiation via straight-through estimator (STE) [3] and chain rule.

1) For $B_{s,l}$,

$$\frac{\partial L_{task}}{\partial \hat{B}_{s,l}} = \frac{\partial L_{task}}{\partial B_{s,l}} = \sum_{\tau} \sum_j \frac{\partial L_{task}}{\partial S_{out,l}^{\tau}} \cdot g_{s,scale} \cdot g_q, \quad (17)$$

$$g_q = \begin{cases} sign(\frac{v_l^t}{V_{th,l}^1}) \cdot (q_{max} + 1) \cdot \ln 2, & \frac{v_l^t}{V_{th,l}^1} > q_{max} \\ 0, & \text{otherwise.} \end{cases} \quad (18)$$

Here, j is the index of the feature map element. The minimum quantization integer $q_{min} = 0$ and the maximum integer $q_{max} = 2^{B_{s,l}} - 1$. While, $g_{s,scale}$, equal to $\frac{1}{\sqrt{\sum_j 1 \cdot q_{max}}}$ and meant to avoid gradient explosion [13], is the gradient scaling factor. L_{task} represents the task loss signal.

2) For $B_{w,l}$,

$$\frac{\partial L_{task}}{\partial \hat{B}_{w,l}} = \frac{\partial L_{task}}{\partial B_{w,l}} = \sum_i \frac{\partial L_{task}}{\partial w_q^l} \cdot g_{w,scale} \cdot g_q, \quad (19)$$

$$g_q = \begin{cases} sign(\frac{w_l}{S_q^l}) S_q^l \cdot (q_{max} + 1) \cdot \ln 2, & \frac{w_l}{S_q^l} \notin [q_{min}, q_{max}] \\ 0, & \text{otherwise.} \end{cases} \quad (20)$$

Specially, when $B_{w,l} = 1$, $q_{min} = -1$ and $q_{max} = 1$. Otherwise, $q_{min} = -2^{B_{w,l}-1} + 1$ and $q_{max} = 2^{B_{w,l}-1} - 1$. Similarly, i is the index of the weight element, and $g_{w,scale} = \frac{1}{\sqrt{\sum_i 1 \cdot q_{max}}}$.

3) For $V_{th,l}^1$ and S_q^l , the derivation of gradients is similar to prior arts [13] and trivial, so we defer it to the appendix.

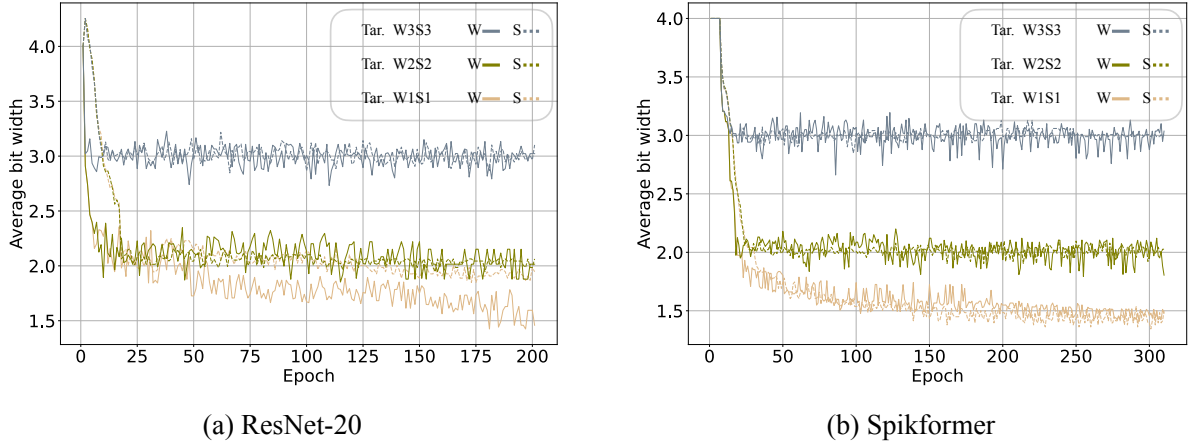


Figure 3: Average bit width changes of ResNet-20 and Spikformer on CIFAR-10 during the adaptive-bit-width training. Tar. abbreviates target bit width. W and S denote weight and spike bit width, respectively.

4) For $S_{out,l}^t$ and T_l , the only non-differentiable terms are the flooring and clipping of Equation 15. We solve them by:

$$\frac{\partial S_{out,l}^t}{\partial (v_l^t/V_{th,l}^1)} = \begin{cases} 1, v_l^t/V_{th,l}^1 \in [q_{min}, q_{max}] \\ 0, \text{otherwise.} \end{cases} \quad (21)$$

q_{min} and q_{max} are in line with the case 1). Thus, $\frac{\partial L_{task}}{\partial S_{out,l}^t}$ and $\frac{\partial L_{task}}{\partial \hat{T}_l}$ can be easily derived via the trivial chain rule.

4.3.2. Loss function

With the above gradient calculations, the bit-width parameters $\hat{B}_{s,l}$, $\hat{B}_{w,l}$, and \hat{T}_l can directly obtain the task loss signal L_{task} for optimization. However, L_{task} alone does not guarantee that these bit-width parameters can be compressed towards the target bit widths. Therefore, we exploit a direct constraint on the average bit width of the model in the following:

$$L_{total} = L_{task} + \lambda_1 L(\bar{B}_w, B_w^{tar}) + \lambda_2 L(\bar{T}, T^{tar}) + \lambda_3 L(\bar{B}_s, B_s^{tar}), \text{ where } L(x, y) = \|x - y\|_2^2. \quad (22)$$

B_w^{tar} , T^{tar} , and B_s^{tar} represent the target bit widths. λ_1 , λ_2 , and λ_3 are penalty coefficients. \bar{B}_w is the average bit width of each weight parameter. \bar{T} and \bar{B}_s are feature element's average time-step and bit width, respectively.

4.4. Quantization step-size renewal

4.4.1. Quantization step size mismatch issue

Bit width is changeable due to parametrization. If it decreases after the previous parameter update, the current quantization step size in the next forward pass will become mismatched. Because the change of bit width belongs to integer mutation while step size does not. Consequently, the quantization error would be increased.

Assuming a variable x , e.g., the activation after convolution, submits to $N(0, \sigma^2)$ and is then filtered via ReLU. Then, only $x > 0$ needs to be considered because $x = 0$ will not incur any quantization error. We get $x \sim 2N(0, \sigma^2)|x > 0$.

Thus, we can offer a theoretical formulation and analysis of the step-size mismatch issue.

Theorem 1. In the quantization process of the variable x : $x_q = s \cdot clip(\lfloor \frac{x}{s} \rfloor, 0, 2^b - 1)$, where $x \sim 2N(0, \sigma^2)|x > 0$; b and s respectively denote the bit width and the quantization step size. Let the quantization step size s be the statistically optimal: $3\sigma = s \cdot (2^b - 1) \Rightarrow s = \frac{3\sigma}{2^b - 1}$ and the quantization error $Err = (x - x_q)^2$. If b decreases to b' , the quantization error would increase by the possibility of $P(x > \frac{2^{b'} - 1}{2^b - 1} \cdot 3\sigma | (x \sim 2N(0, \sigma^2), x > 0))$. (Theorem and proof of the bidirectional domain, i.e., no ReLU applied and $x \sim N(0, \sigma^2)$, are in the appendix.)

PROOF. Given $b' < b$ and $x'_q = s \cdot clip(\lfloor \frac{x}{s} \rfloor, 0, 2^{b'} - 1)$, we obtain $x'_q = x_q - \lambda$, where $\lambda = s[clip(\lfloor \frac{x}{s} \rfloor, 2^{b'} - 1, 2^b - 1) - (2^{b'} - 1)]$. Thus, $Err' = (x - x_q + \lambda)^2$, and the possibility of $P(Err' > Err)$ equates to $P(\lambda > 0)$ (the deduction here is deferred to the appendix). We can get

$$\begin{aligned} P(\lambda > 0) &= P(\frac{x}{s} > 2^{b'} - 1) \\ &= P(x > \frac{2^{b'} - 1}{2^b - 1} \cdot 3\sigma). \end{aligned} \quad (23)$$

We conclude that **I)** a larger decrease in bit width leads to a higher possibility of increased quantization error.

Lemma 1. Because $b' \leq b - 1$ and $b' \geq 1$, we get $\frac{2^{b'} - 1}{2^b - 1} \leq \frac{1}{2}$. Thus, the lower bound of $P(\lambda > 0)$ can be calculated:

$$P(\lambda > 0) > P(x > \frac{3\sigma}{2}). \quad (24)$$

Since $x \sim 2N(0, \sigma^2)$ and $x > 0$, we obtain $P(x > \frac{3\sigma}{2}) = 0.1336 > 0$. Consider a tensor $X = \{x_1, x_2, \dots\}^n$, we can conclude that **II)** as bit width decreases, the unchanged step size would inevitably incur more quantization errors when X has a large dimension n .

Algorithm 1 Step-size renewal algorithm.

Initialize the bit-width observer: The running maximum V_{r_max} is set to $-\infty$ and the minimum V_{r_min} is set to ∞ . The recorded bit width B'_l is set to 0.

Input: Data to be quantized X and X 's current bit width B_l .

Output: The optimal S_l .

```

1: if  $B_l \neq B'_l$  do
2:    $B'_l \leftarrow B_l$ 
3:   if  $X$  is defined in the bidirectional domain do
4:      $q_{min} \leftarrow -2^{B'_l-1} + 1$ 
5:      $q_{max} \leftarrow 2^{B'_l-1} - 1$ 
6:   else do
7:      $q_{min} \leftarrow 0$ 
8:      $q_{max} \leftarrow 2^{B'_l} - 1$ 
9:    $V_{max}, V_{min} \leftarrow \max(X), \min(X)$ 
10:   $V'_{max}, V'_{min} \leftarrow \text{Input}(X, V_{min}, V_{max})$  to Algorithm 2.
11:   $V_{r\_max}, V_{r\_min} \leftarrow \max(V'_{max}, V_{r\_max}), \min(V'_{min}, V_{r\_min})$ 
12:   $S_l \leftarrow \frac{V_{r\_max} - V_{r\_min}}{q_{max} - q_{min}}$ 
13:  return  $S_l$ 
14: else do
15:  pass
    
```

With the conclusion **I**) and **II**) combined, the step-size mismatch issue can be proven harmful in direct training, where bit-width mutation constantly occurs between forward passes as shown in Figure 3. As the model goes deeper, quantization error accumulates and seriously impairs the model output [38]. *The step size mismatch influence could be more severe in SNNs because the invalid step size will be consecutively used along the temporal dimension in Equation 5.* Therefore, the quantization error will accumulate temporally, causing serious inference offsets. For instance, if $X = \{x_1, x_2, \dots, x_T\}$, then the possibility of a increased quantization error $(X - X_q)^2$ would be $1 - [1 - P(x > \frac{2^{b'_l}-1}{2^{b-1}}3\sigma)]^T$, which increases as T rises.

4.4.2. Step-size renewal mechanism

To alleviate the mismatch issue, we propose the following step-size renewal. As illustrated in Figure 2, the renewal mechanism is based on a bit-width observer that watches on the bit width B_l , e.g., $B_{w,l}$ and $B_{s,l}$, and records the running maximum V_{r_max} and minimum V_{r_min} of the data to be quantized. V_{r_max} and V_{r_min} , reflecting the overall data distribution, will be used to renew the step size S_l , e.g., S_q^l and $V_{th,l}^1$, directly.

As illustrated in Algorithm 1, once B_l is changed, the new B_l will be recorded, the new q_{max} and q_{min} are calculated accordingly, and the observer will also instantly read the current maximum V_{max} and minimum V_{min} of the current batch of data X , e.g., weight or activation. Based on V_{max} and V_{min} , a grid search is performed to calculate the currently optimal maximum V'_{max} and minimum V'_{min} as written in Algorithm 2. Finally, the running maximum V_{r_max} and

Algorithm 2 Grid search on V_{max} and V_{min} .

Input: Data to be quantized X , the V_{max} and V_{min} of X , the iteration number K , the minimum quantization integer q_{min} , the maximum quantization integer q_{max} , and the power constant pow .

Output: The optimal V'_{max} and V'_{min} .

```

1:  $Score \leftarrow 0, R \leftarrow V_{max} - V_{min}, V'_{max} \leftarrow V_{max}$ , and  $V'_{min} \leftarrow V_{min}$ .
2: for  $k = 1; k \leq K; i++$  do
3:    $V_{max} \leftarrow \frac{k \cdot R}{K}$ 
4:   if  $\text{any}(X < 0)$  do
5:      $V_{min} \leftarrow -\frac{k \cdot R}{K}$ 
6:   else do
7:      $V_{min} \leftarrow 0$ 
8:    $S'_l \leftarrow \frac{V_{max} - V_{min}}{q_{max} - q_{min}}$ 
9:    $X_{q,k} \leftarrow S'_l \cdot \text{clip}\left(\frac{X}{S'_l}, q_{min}, q_{max}\right)$ 
10:   $Score' \leftarrow \text{mean}(|X_{q,k} - X|^{pow})$ 
11:  if  $Score' < Score$  do
12:     $Score \leftarrow Score'$ 
13:     $V'_{max}, V'_{min} \leftarrow V_{max}, V_{min}$ 
14: return  $V'_{max}, V'_{min}$ 
    
```

$\text{mean}(x)$ is the element-wise averaging function. $\text{any}(x)$ checks if at least one element is True.

minimum V_{r_min} are updated via

$$\begin{aligned} V_{r_max} &= \max(V'_{max}, V_{r_max}), \\ V_{r_min} &= \min(V'_{min}, V_{r_min}). \end{aligned} \quad (25)$$

And, the renewed step size S_l is determined via

$$S_l = \frac{V_{r_max} - V_{r_min}}{q_{max} - q_{min}}. \quad (26)$$

Thus, an optimal S_l can be applied and cover the original one to correct the current forward pass. Since the grid search process will consume extra training time, we only activate the renewal mechanism in the drastic bit reduction stage. Based on the observations of Figure 3, bit reduction mainly occurs in the first 12.5% epochs. Therefore, we set a shutting threshold that once the difference between the current and the target bit width is below 24% of the initial difference, the renewal mechanism would be deactivated. Consequently, the training time increased by the grid search is lower than 0.05% of the total training time.

5. Experiments

In this section, we first compare our methods with the existing works using ResNet on CIFAR [27] and ImageNet-1k [9], then conduct ablation studies to verify different aspects of our methods, including **(1)** each proposed technology's verification, **(2)** our methods' extension to spiking self-attention [56], **(3)** mitigating the "temporal constraint" of the prior arts [39] on the event dataset CIFAR10-DVS [28] and DVS-GESTURE [2], **(4)** extending to the spiking

Table 1

Comparisons with existing works on CIFAR. W/S/T denotes the averaged weight/spike/temporal bit width. U-Quant., following [39], is the plain uniform quantization on SNN, which uses fixed uniform bit widths. Our models are initial to W/S/T=4/4/2.

Method	Architecture	CIFAR 10					CIFAR 100				
		W/S/T	Bit Budget	S-ACE (G)	Size (MB)	Top-1	W/S/T	Bit Budget	S-ACE (G)	Size (MB)	Top-1
Dspike [29]	ResNet18	16/1/2	32	17.72	22.42	93.13	16/1/2	32	17.72	22.42	71.68
		16/1/4	64	35.44	22.42	93.66	16/1/4	64	35.44	22.42	73.35
MLF [16]	ResNet20	16/1/4	64	165.58	34.55	94.25	16/1/4	64	165.58	34.55	-
tdBN [55]	ResNet19	16/1/2	32	73.28	25.25	92.34	16/1/2	32	73.28	25.25	-
		16/1/4	64	146.56	25.25	92.92	16/1/4	64	146.56	25.25	-
TET [11]	ResNet19	16/1/2	32	73.28	25.25	94.16	16/1/2	32	73.28	25.25	72.87
		16/1/4	64	165.12	25.25	94.44	16/1/4	64	165.12	25.25	74.47
Ternary Spike [18]	ResNet19	16/2/1	32	330.24	25.25	95.58	16/2/1	32	330.24	25.25	78.45
	ResNet20	16/2/2	64	165.58	34.55	94.48	16/2/2	64	165.58	34.55	73.41
		16/2/4	128	330.24	34.55	94.96	16/2/4	128	330.24	34.55	74.02
Multi-bit Spike [48]	ResNet20	16/4/1	64	165.58	34.55	94.59	16/4/1	64	165.58	34.55	75.43
		16/4/4	256	660.48	34.55	94.93	16/4/4	256	660.48	34.55	76.51
		16/4/6	384	990.72	34.55	95.00	16/4/6	384	990.72	34.55	-
U-Quant.†	ResNet20	4/4/1	16	41.40	8.64	96.35	4/4/1	16	41.40	8.64	79.83
		4/4/2	32	82.79	8.64	96.39	4/4/2	32	82.79	8.64	80.19
Ours-111	ResNet18	1.45/1.61/1.04	2.43	2.96	2.03	95.13	1.65/1.87/1.03	3.17	4.29	2.32	75.42
Ours-222		1.97/2.04/2.01	8.1	11.59 / 6.56*	2.75	96.01	2.06/2.08/2.02	8.69	11.34 / 6.86*	2.89	75.80
Ours-111	ResNet20	1.38/1.32/1.00	1.83	7.55	2.98	96.15	2.06/1.58/1.00	3.25	13.37	4.45	79.70
Ours-222		2.13/2.00/2.08	8.87	29.75 / 15.93*	4.60	96.48	2.11/1.98/2.08	8.66	32.67 / 18.83*	4.56	80.59
Ours-341		3.01/4.00/1.00	12.08	39.49	6.51	97.02	2.88/4.04/1.00	11.64	40.60	6.23	81.30

† denotes plain uniform quantization, following [39]. * denotes the temporal squeezing is applied in inference. "Ours-xxx" denotes the target bit widths of W/S/T.

Table 2

Comparisons with existing works on ImageNet.

Method	Architecture	W/S/T	Bit Budget	S-ACE (G)	NS-ACE(G)	Size (MB)	Top-1
Hybrid training [36]	ResNet34	16/1/250	4000	13608	-	43.56	61.48
Spiking ResNet [23]	ResNet50	16/1/350	5600	18952	-	51.12	72.75
tdBN [55]	ResNet34	16/1/6	96	340.39	-	43.56	63.72
Dspike [29]	ResNet34	16/1/6	96	340.39	-	43.56	68.19
MS-ResNet [22]	ResNet34	16/1/6	96	340.39	-	43.56	69.42
Attention-SNN [52]	ResNet34	16/1/1	16	56.73	-	43.56	69.15
TET [11]	Sew-ResNet34	16/1/4	64	226.93	-	43.56	68.00
Ternary Spike [18]	ResNet34	16/2/4	128	435.86	-	43.56	70.74
PLIF+SEW [15]	SEW-ResNet34	16/1/4	64	226.93	63.14	43.56	67.04
	SEW-ResNet50	16/1/4	64	215.62	69.03	51.12	67.78
Quant. SNN [39]	SEW-ResNet34	8/8/1	64	226.93	56.42	21.78	70.13
Ours-221		2.58/2.18/1.0	5.61	30.74	7.77	7.03	70.57
Ours-241	SEW-ResNet34	2.62/3.96/1.0	10.39	54.69	16.99	7.14	72.02
Ours-441		3.93/3.92/1.0	15.4	77.78	24.30	10.69	72.82

Table 3

Ablations on adaptive bit width and the renewal mechanism. Different fonts denote the **first**, the **second**, and the **third** best results, respectively. Our bit-adaptive models are initial to W/S/T=4/4/2.

Target	U-quant.	Bit-adaptive		Bit-adaptive +Weight-only Renewal		Bit-adaptive +Bilateral Renewal		Bit-adaptive +Act.-only Renewal	
		W/S/T	Top-1	W/S/T	Top-1	W/S/T	Top-1	W/S/T	Top-1
1/1/1	74.82	1.60/1.91/1.0	95.65	1.73/1.98/1.0	93.28	1.25/1.36/1.0	95.84	1.38/1.32/1.0	96.15
1/2/1	86.8	1.48/2.00/1.0	95.55	1.57/2.12/1.0	93.52	1.25/2.04/1.0	96.25	1.42/2.08/1.0	96.58
2/2/1	88.65	1.88/2.06/1.0	94.62	1.99/2.06/1.0	95.71	2.00/1.89/1.0	96.47	2.08/2.08/1.0	96.51
2/3/1	93.64	2.10/3.00/1.0	96.37	1.96/3.00/1.0	96.51	2.02/3.06/1.0	96.97	2.24/3.06/1.0	96.63
3/3/1	95.38	3.01/2.95/1.0	96.34	3.00/3.06/1.0	96.66	2.87/3.04/1.0	96.77	2.89/2.87/1.0	96.90
3/4/1	96.09	2.87/4.10/1.0	96.72	2.90/3.98/1.0	96.89	2.97/3.94/1.0	97.01	3.01/4.00/1.0	97.02
4/4/1	96.35	4.04/4.06/1.0	96.78	3.99/4.02/1.0	97.00	3.86/4.00/1.0	97.03	3.99/4.06/1.0	97.05
4/4/2	96.39	4.02/3.93/1.92	96.80	3.88/4.04/2.0	96.57	4.01/3.97/2.0	97.03	3.93/4.03/2.08	96.92

audio task SHD [8], (5) the learned bit allocation’s visualization, and (6) comparing the mixed-precision ANNs. All implementation details are attached in the appendix.

5.1. Comparisons with existing works

5.1.1. CIFAR

We apply our methods to ResNet20 [18] and ResNet18 [29] to compete with the advanced SNNs. As shown in Table 1, we first compare our methods with those using extra learning- or module-based model optimization [29, 11, 55], and achieve superior accuracy using much lower memory (bit budget) and computation (S-ACE). In the case of ResNet-18 with target W/S/T being 1/1/1, our methods can also compress the model sizes to one-tenth of their original dimensions, while achieving at most 2% and 3.74% higher model accuracy on CIFAR-10 and CIFAR-100, respectively. Such a reduction of storage requirements would make SNNs more compatible with on-chip computing architectures [1, 34]. Comparing with Ternary Spike ResNet20 [18] that adopts 2-bit bidirectional spike, we can outperform it by at least 1.19% and 5.88% accuracy increase on CIFAR-10 and -100, respectively, while using average 1.32- and 1.58-bit spike and reducing 91.37% and 90.59% model sizes. Then, we compare with Multi-bit ResNet20 [48], whose memory and computation respectively increase to huge 256 bit budgets and 660.48 G S-ACEs. While, our model can achieve not only 1.22% and 3.39% accuracy increase on CIFAR-10 and CIFAR-100 but also two magnitudes of memory and computation savings. Finally, compared with plain uniform quantization (U-quant.), our methods can maximize the model accuracy while minimizing memory and computation requirements. The advantages of our approaches in terms of memory usage, computational efficiency, and storage requirements are consistently demonstrated. Additionally, since we adopt temporal squeezing as shown in Figure 2 and Equation 13, the temporal dimension can be compressed to 1 time-step before operating convolution. That is why S-ACE can further decrease when "W/S/T=222" and more elaborations are in the appendix for better understanding. In conclusion, by comparing with state-of-the-art methods on CIFAR-10 and CIFAR-100, we demonstrate significant improvements in memory efficiency, computational requirements, and storage consumption.

5.1.2. ImageNet

We further apply our methods to SEW-ResNet34 to demonstrate superiority on the up-scaled dataset. As listed in Table 2, compared with those using improved learning techniques or special modules [36, 55, 29, 22], we can achieve magnitudes of memory and computation savings without using any of their tricks. Attention SNN [52] has comparable S-ACE (56.73 G) with ours (30.74 G and 54.69 G), but its memory efficiency, model accuracy, and storage requirement lag far behind those of our methods. We can achieve at least 1.42% increased accuracy while reducing 45.81% S-ACE and 83.86% model size. Besides, our models would not require sophisticated attention modules [52] as they do, which indicates a more straightforward inference

dataflow and a better computing flow mapping from software to hardware. Furthermore, we can save 91.2% memory (5.61 v.s. 64) and 85.83% computation (30.74 G v.s. 217 G) while achieving a higher accuracy (70.57% v.s. 70.13%) when comparing with the quantized SNN [39]. As the bit budget increases, the model accuracy can be advanced to 72.82% with low memory and computation overheads, outperforming full-precision SNNs [18, 15, 11]. Conclusively, scaling our model to the large ImageNet-1k dataset further demonstrates the effectiveness of the proposed methods in improving the efficiency and accuracy of SNNs.

5.2. Ablation study

We first continue to use ResNet20 and CIFAR10 to conduct ablation studies on the proposed techniques. Then, we migrate the proposed method to a different architecture, Spikformer [56], to further verify effectiveness. On the extension to the event dataset, we leverage our methods to mitigate the "temporal constraint" issue, which troubles the prior art [39]. We also extend our methods to the spiking audio task SHD [8] by incorporating the axonal delay mechanism [40, 20] Furthermore, we provide visualizations of the learned bit allocation as empirical evidence and statistically analyze the results. Finally, we compare our bit-adaptive SNNs with the ANN baselines to show the superiority of SNNs in scenarios of ultra-low-energy computation. Notably, since our work targets building efficient and accurate SNNs, we mainly focus on the effectiveness of the proposed approaches under the low bit budget settings and conduct ablation studies in this background.

5.2.1. Effectiveness of adaptive bit width and the renewal mechanism

We first perform the plain uniform quantization on SNNs (U-quant.) as the baselines, following [39]. As shown in Table 3, the proposed adaptive bit-width technology consistently outperforms U-quant., managing to allocate valid bit widths to different layers and improving the model accuracy to a higher level. Furthermore, we add the proposed renewal mechanism only to the spike activation ($V_{ih,l}^1$, Act.-only), or only to the weight (S_q^l , Weight-only), or to the bilateral case ($V_{ih,l}^1$ and S_q^l). The results coherently show the renewal mechanism can further improve the outcomes of the bit-adaptive models, mitigating the step-size mismatch issue. As described before, SNN’s activation would accumulate quantization errors along the temporal dimension. That is why Act.-only renewal is effective enough to produce the best results. Bilateral renewal seconds due to a slightly lower bit budget. For simplicity, we adopt the Act.-only renewal as the main method by default.

In addition, another interesting finding is that the results of the target W/S/T=4/4/1 are better than those of the target W/S/T=4/4/2. This may imply that more temporal information contribute limited improvement or even cause over-fitting to the processing of static data when spatial information is efficiently provided and processed.

Table 4

Ablations on the refined spiking neuron. Different fonts denote the **first**, the **second**, and the **third** best results, respectively.

Target	$\tau = 2$ & Flooring	$\tau = 2$ & Flooring		$\tau = 2$ & Flooring		$\tau = 2$ & Rounding		$\tau = 1$ & Rounding	
	U-quant.	w/o renewal		w/ renewal		w/ renewal		w/ renewal	
W/S/T	Top-1	W/S/T	Top-1	W/S/T	Top-1	W/S/T	Top-1	W/S/T	Top-1
1/1/1	74.82	1.80/2.14/1.0	95.12	1.80/2.09/1.0	95.58	1.46/1.34/1.0	95.71	1.38/1.32/1.0	96.15
1/2/1	10.02	1.77/2.2/1.0	95.21	1.58/2.13/1.0	<u>96.14</u>	1.40/2.05/1.0	96.48	1.42/2.08/1.0	96.58
2/2/1	0.1	2.10/2.07/1.0	95.50	2.09/1.97/1.0	<u>96.04</u>	1.88/1.95/1.0	96.45	2.08/2.08/1.0	96.51
2/3/1	89.06	2.05/3.01/1.0	<u>96.51</u>	2.13/3.16/1.0	96.38	1.96/3.04/1.0	96.72	2.24/3.06/1.0	96.63
3/3/1	0.1	2.98/3.02/1.0	<u>96.18</u>	3.01/3.07/1.0	<u>96.43</u>	3.03/3.01/1.0	96.82	2.89/2.87/1.0	96.90
3/4/1	96.31	3.06/3.98/1.0	96.64	2.99/4.02/1.0	<u>96.80</u>	2.95/4.06/1.0	97.00	3.01/4.0/1.0	97.02

Table 5

Ablations of Spikformer-4-384 on CIFAR10. Different fonts denote the **first** and the **second** best results, respectively.

Target	U-quant.	Bit-adaptive		Bit-adaptive + renewal		Origin [56]	
	W/S/T	Top-1	W/S/T	Top-1	W/S/T	Top-1	W/S/T
1/1/1	79.53	1.44/1.48/1.0	95.37	1.53/1.5/1.0	95.47		
1/2/1	89.3	1.47/1.99/1.0	95.68	1.47/2.01/1.0	<u>95.54</u>		
2/2/1	89.68	1.88/2.03/1.0	95.80	2.02/2.01/1.0	95.84	16/1/4	95.19
2/3/1	94.11	2.00/2.94/1.0	95.93	2.15/2.95/1.0	96.04		
3/3/1	94.21	2.93/3.01/1.0	95.87	2.89/2.99/1.0	95.99		

U-quant. denotes plain uniform quantization, following [39].

5.2.2. Importance of the refined spiking neuron

We further verify the effectiveness of the refined spiking neuron. Key improvements over prior multi-bit spiking neurons [18, 48] include: (1) refining Equation 5 to Equation 15 by replacing flooring with rounding, and (2) adopting the IF neuron ($\tau = 1$) instead of the default LIF neuron ($\tau = 2$) [14]. In Table 4, the results consistently show that the original multi-bit neuron would impair the quantized model’s robustness, whereas our refinement method and renewal mechanism steadily improve the model performance to better states. This enables the development of high-performance and low-overhead SNNs.

Another insight might also be drawn. In the field of deep learning, the value quantizer regulates information widths of features and consequently reduce the redundant data movement and computing operations in the following layer. The firing mechanism in the LIF model emulates biological neurotransmission by transforming chemical stimuli into electrical impulses, achieving energy-efficient information transfer [17]. Therefore, the firing mechanism is the key to generating the efficient value representation, i.e., low-bit value, to achieve energy-efficient computing as the value quantizer does. Previous works [46, 23, 19] on direct-trained SNNs directly adopted the mathematical formulation of the LIF model without adapting it to the intrinsic characteristics of deep learning computations, which potentially compromises the network performance. After introducing the concept of quantization error and adhering to the principle of minimizing quantization errors, we refined the LIF model, thereby achieving further performance enhancements in SNNs. In conclusion, although SNN is a bio-inspired model, reducing

the quantization error is still important in maintaining SNN’s good model performance.

5.2.3. Validation on spiking self-attention architectures

Migrating our methods to Spikformer is non-trivial because the self-attention operation is a different computing paradigm where a new quantizable tensor *atten* (see Figure 2(a)) is produced. We would like to leave room for future work. Here, we naively apply our methods to Spikformer as depicted in Figure 2 only to validate the migratability and effectiveness of the proposed methods, and avoid competing with those state-of-the-art works that are based on sophisticated spiking self-attention architectures. We adopt the default Spikformer-4-384 [56] on CIFAR10. In Table 5, our bit-adaptive model surpasses the original Spikformer, while plain uniform quantization fails. Besides, adding the renewal mechanism further lifts accuracy.

5.2.4. Mitigating the temporal constraint

We further test the migratability of the proposed methods on the event datasets. We use the same default Spikformer and settings as [39] without data augmentation. As shown in Table 6, "temporal constraint" refers to the dramatic accuracy decrease of event datasets as temporal length declines to the extremely low time-step [39]. However, in our work, such a phenomenon disappears and accuracy is well maintained even in the case of $T = 1$. This implies that our methods can better extract spatial information even in sparse event data. Meanwhile, we are in line with prior findings that temporal length would maintain a notable effect on accuracy for event datasets. Moreover, compared with the original Spikformer,

Bit-adaptive Spiking Neural Networks

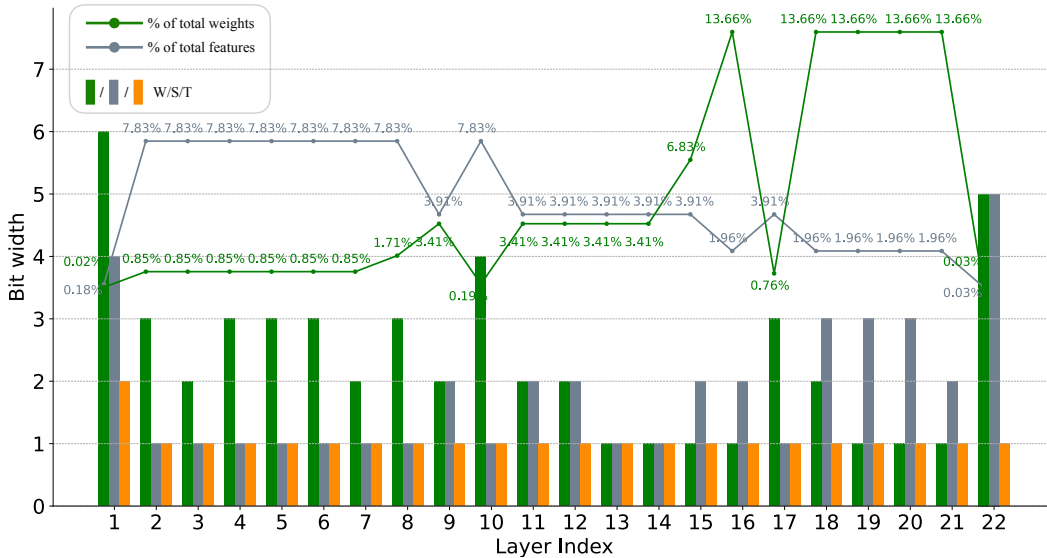


Figure 4: Statistics of each layer’s bit widths. Since layer #1 has two time-steps, we report the averaged spike bit width for clarity.

Table 6

Spikformers on CIFAR10-DVS. The best results and temporal lengths are highlighted.

Origin [39]		Quantized Spikformer [39]		Our Spikformer	
W/S/T	Top-1	W/S/T	Top-1	W/S/T	Top-1
		1/1/16	79.8	1.11/2.00/6.0	80.9
		1/2/8	79.3	1.28/2.00/4.0	80.0
16/1/16	80.7	1/4/4	63.1	1.33/4.00/3.0	80.1
		1/8/2	43.0	1.31/4.03/2.0	78.7
		1/16/1	35.8	1.31/4.03/1.0	77.4

Table 7

Spikformers on DVS-GESTURE. The best results and temporal lengths are highlighted.

Origin [39, 56]		Quantized Spikformer [39]		Our Spikformer	
W/S/T	Top-1	W/S/T	Top-1	W/S/T	Top-1
		1/1/16	96.67	1.17/2.18/6.0	99.31
		1/2/8	98.48	1.29/2.08/4.0	98.61
16/1/16	98.3	1/4/4	97.35	1.32/4.00/3.0	97.92
		1/8/2	96.59	1.31/4.00/2.0	97.57
		1/16/1	95.45	1.37/4.00/1.0	96.18

our methods can achieve higher accuracy with lower bit budgets and time-steps, proving the effectiveness on event data.

Futhermore, another mainstream event-based dataset DVS-GESTURE [2] is smaller and easier for models to converge, and the "temporal constraint" issue does not manifest. In this case, our model can still significantly strengthen the temporal processing ability of SNNs. As listed in Table 7, our model can achieve consistently better accuracy while using shorter time lengths and fewer bit budgets when compared with the baseline models. In the case of W/S/T = 1.17/2.18/6.0, our model can achieve advanced 99.31 % top-1 accuracy. To the best of our knowledge, this should be a state-of-the-art result of SNNs on the dynamic dataset.

5.2.5. Extension to the spiking audio task

Instead of focusing solely on the event image datasets, including CIFAR10-DVS and DVS-GESTURE, we also extend our methods to the spiking audio dataset SHD [8]. However, directly applying SNNs to the spiking audio dataset will cause significant performance loss [40]. Prior arts have proposed that the axonal delay mechanism can solve this issue [40, 20]. Therefore, we utilize the dilated convolution with learnable spacings (DCLS) [20] to implement the axonal

Table 8

Extended experiments on the spiking audio dataset SHD.

Method	Parameters (M)	Top1
DMUC [41]	0.24	91.48
CNN [8]	1.01	92.40
RSNN [8]	1.97	83.20
Attention RSNN [51]	0.14	91.08
RadLIF [4]	3.9	94.62
DL256-SNN-Dloss [40]	0.21	93.55
DCLS [20]	0.21	95.07
Our DCLS-3.5/1/25	0.21	95.17
Our DCLS-4.4/1/25	0.21	95.54

"Ours DCLS-x/x/x" denotes the learned bit widths of W/S/T.

Following the research tradition of spiking audio tasks, we only report the parameter numbers (M) instead of the model size (MB).

delay. Instead of directly adopting the local spike connection, which may require some modifications on the spiking neuron formulation [40], to realize axonal delays, DCLS utilizes the temporal-wise 1D convolution to implement the axonal delay mechanism. This means DCLS only operates on spiking

Table 9
Additional comparisons with mixed-precision ANNs.

Target W/A(S)/T	Mixed-precision ANN [42]		Our bit-adaptive SNN	
	W/A	Top-1	W/S/T	Top-1
1/1/1	1.48/1.93	95.78	1.25/1.36/1.0	95.84
1/2/1	1.48/2.03	95.68	1.25/2.04/1.0	96.25
2/2/1	1.92/2.07	95.71	2.00/1.89/1.0	96.47
2/3/1	2.19/3.05	96.29	2.02/3.06/1.0	96.97
3/3/1	3.13/2.97	96.56	2.87/3.04/1.0	96.77
3/4/1	3.07/3.98	96.97	2.97/3.94/1.0	97.01
4/4/1	3.87/3.96	96.76	3.86/4.00/1.0	97.03

The results of mixed-precision ANNs [42] are produced by re-implementing their paper.

feature maps without introducing any modification to our refined spiking neurons.

As shown in Table 8, our method not only outperforms the DCLS baseline, but also achieves the state-of-the-art (SoTA) model accuracy on the SHD dataset. This result shows our bit-adaptive SNNs are compatible with the axonal delay mechanism, and can significantly improve the SNN performance when handling the spiking audio data.

5.2.6. Statistics of bit widths

We visualize the learned bit allocation of ResNet20 with $W/S/T = 1.38/1.32/1$ on CIFAR10 to visually confirm the effectiveness. Notably, different from any prior arts [18, 55, 15], we add additional spiking neurons before the first layer to fully benefit the model with addition-only computation. In consistence with the previous setting, the model is initialized to $W/S/T = 4/4/2$. As vividly displayed in Figure 4, **I)** the layers with the higher proportion of features and weights tend to get lower bits thus lowering the overall memory and computation. **II)** The first and last layers tend to learn higher bit widths in line with their outstanding importance as reported in prior arts [7]. With **I)** and **II)** combined, we conclude our adaptive bit allocation method should be sensible and practical.

5.2.7. Additional comparisons with mixed-precision ANNs

Since we use a similar bit-width parametrization and gradient calculation to the mixed-precision ANN [42], we also need to conduct a fair comparison with mixed-precision ANNs. Here, we continue using ResNet20 on CIFAR10.

As listed in Table 9, our proposed adaptive bit allocation SNNs consistently outperform the mixed-precision ANNs under every $W/S/T$ setting. In the case of extremely low bit widths, e.g., the target $W/S/T=1/1/1$, our SNN can achieve higher accuracy while using a lower bit budget. This implies that SNNs may have an advantage over ANNs in scenarios of ultra-low-energy computation, which is in line with previous studies [10, 21].

Additionally, our SNN has adopted the proposed renewal mechanism and a bit different gradient calculations (see Section 4.3.1). Therefore, Table 9 can also imply the effectiveness of our proposed methods as a whole.

6. Discussion

The most precious characteristic that SNN brings is its asynchronous processing ability, i.e., event-driven and clock-free computing. We would like to address the potential concerns about how such nature and merit could be maintained when temporal squeezing is applied.

Exploiting the spike perceptrons. Temporal squeezing itself is consistent with neurodynamics as it is essentially composed of a signal accumulation [17] and a division operation. A similar accumulation mechanism can also be found in the current accumulation stage of spiking neuron, such as LIF and IF. Particularly, SpikeConverter neuron [32] separates this accumulation from the spiking neuron modeling and uses a special computing pipeline to handle this accumulation. Their accumulation is identical to ours, which is proven feasible in asynchronous computing. In addition, such accumulation has also been realized and implemented by neuromorphic circuits to process the DVS signals and generate the dynamic datasets [2, 31].

Using the two-stage pipeline. Although we have theoretically elaborated on the harmlessness of temporal squeezing to the asynchronous nature in the above, one may argue that the entire network’s spike flow could be interrupted by the squeezing stage, leading to longer inference latency. This concern has already been discussed and resolved by [32], where the two-stage pipeline is adopted. The first stage is spike accumulation, i.e., the temporal squeezing, the second stage is spike emission. These two separate stages can overlapped inter-layer. Therefore, using temporal squeezing only introduces very limited latency increase.

7. Conclusion

In this paper, we propose an adaptive bit allocation method, based on learnable bit widths, for efficient and accurate SNNs. To resolve the new challenges brought by the temporal dimension of SNN, we refine the spiking neuron to enable temporal matching inter-layer and intra-layer, and increase the adaptivity via the better neuron formulation and hyperparameter. We further formulate the step-size mismatch issue that would temporally deteriorate, and alleviate it through the proposed renewal mechanism.

Extensive experiments are conducted to demonstrate the effectiveness of the proposed methods on the static CIFAR-10, CIFAR-100, and ImageNet datasets and the dynamic CIFAR10-DVS and DVS-GESTURE datasets. Not only is the model accuracy improved with our approaches, but the memory (bit budget) and the computation overhead (S-ACE) are also significantly reduced. Ablation studies further prove the effectiveness of every proposed technique. Results on the dynamic datasets show our methods can further help SNNs resolve the temporal constraint issue that troubles the previous work. The effectiveness and rationality of our methods are also empirically validated through statistical visualization. Additional comparisons with the ANN baseline also imply that SNNs may have an advantage over ANNs in scenarios of ultra-low-energy computation.

Acknowledgements

This work was supported by State Grid Corporation of China, Science and Technology Project under grant No.5700-202358838A-4-3-WL.

A. My Appendix

A.1. Guideline

In this technical appendix, we provide the following supplementary materials for the main text:

1. Section A.2: **(I)** the proof of the fact that *the flooring operation would incur more quantization error than the rounding operation*, **(II)** the full deduction of **Proof 1**, and **(III)** the proof of **Theorem 1** in the bidirectional domain;
2. Section A.3: the gradient calculations of $V_{th,l}^1$ and S_q^l ;
3. Section A.4: the gradient calculations of the bidirectional-spike version of the learnable bit width ($B_{s,l}$) and quantization step size ($V_{th,l}^1$); to $V_{th,l}^1$ and $B_{s,l}$;
4. Section A.5: the details of the experimental settings;
5. Section A.6: the elaboration on how temporal squeezing would further reduce the S-ACE when temporal length is over 1;
6. Section A.7: the additional comparisons on ImageNet and CIFAR10-DVS.
7. Section A.8: more elaboration on maintaining the asynchronous nature of SNNs.
8. Section A.9: overall algorithm of the proposed adaptive-bit-allocation training.

A.2. Supplementary proofs

A.2.1. Proof of the flooring operation incurring more quantization errors

Considering the quantization process of the variable x , we assume $x \sim N(0, \sigma^2)$. Then, the flooring quantization process of the variable x would be $x_q^f = s \cdot clip(\frac{x}{s}, -2^{b-1} + 1, 2^{b-1} - 1)$, where s and b are the quantization step size and the bit width, respectively. Similarly, the rounding quantization process would be $x_q^r = s \cdot clip(\frac{x}{s}, -2^{b-1} + 1, 2^{b-1} - 1)$.

Defining the quantization error as $Err = (x - x_q)^2$, then we get the expectation of the flooring quantization error:

$$\begin{aligned}
 E(Err^f) &= s^2 \left[\sum_{j=0}^{2^b-3} \int_{-2^{b-1}+1+j}^{-2^{b-1}+2+j} \left(\frac{x}{s} - \left\lfloor \frac{x}{s} \right\rfloor\right)^2 \cdot P(x) d\frac{x}{s} \right. \\
 &\quad + s^2 \int_{-\infty}^{-2^{b-1}+1} \left[\frac{x}{s} - (-2^{b-1} + 1)\right]^2 \cdot P(x) d\frac{x}{s} \\
 &\quad \left. + s^2 \int_{2^{b-1}-1}^{+\infty} \left[\frac{x}{s} - (2^{b-1} - 1)\right]^2 \cdot P(x) d\frac{x}{s}, \right. \\
 &\quad \text{where } P(x) = \frac{1}{\sigma\sqrt{2\pi}} e^{-\frac{x^2}{2\sigma^2}} \text{ is the PDF of } x.
 \end{aligned} \tag{A.1}$$

Similarly we get the expectation of the rounding quantization error:

$$\begin{aligned}
 E(Err^r) &= s^2 \left[\sum_{j=0}^{2^b-3} \int_{-2^{b-1}+1+j}^{-2^{b-1}+2+j} \left(\frac{x}{s} - \left\lfloor \frac{x}{s} \right\rfloor\right)^2 \cdot P(x) d\frac{x}{s} \right. \\
 &\quad + s^2 \int_{-\infty}^{-2^{b-1}+1} \left[\frac{x}{s} - (-2^{b-1} + 1)\right]^2 \cdot P(x) d\frac{x}{s} \\
 &\quad \left. + s^2 \int_{2^{b-1}-1}^{+\infty} \left[\frac{x}{s} - (2^{b-1} - 1)\right]^2 \cdot P(x) d\frac{x}{s}. \right.
 \end{aligned} \tag{A.2}$$

For clarity, We simplify the mathematical notation in the following by omitting the upper and lower bounds of the integral symbol. Thus, we get

$$\begin{aligned}
 &E(Err^f) - E(Err^r) \\
 &= s^2 \left\{ \sum_j \int \left[\left(\frac{x}{s} - \left\lfloor \frac{x}{s} \right\rfloor\right)^2 - \left(\frac{x}{s} - \left\lfloor \frac{x}{s} \right\rfloor\right)^2 \right] \cdot P(x) d\frac{x}{s} \right\} \\
 &= s^2 \left\{ \sum_j \int \overbrace{\left[\frac{2x}{s} - \left(\left\lfloor \frac{x}{s} \right\rfloor + \left\lfloor \frac{x}{s} \right\rfloor\right) \right] \left[\left\lfloor \frac{x}{s} \right\rfloor - \left\lfloor \frac{x}{s} \right\rfloor \right]}^{\#} \cdot P(x) d\frac{x}{s} \right\}
 \end{aligned} \tag{A.3}$$

We further discuss # as follows:

1. If $x > 0$ and $\frac{x}{s} \notin \{\mathbb{Z}, \mathbb{Z} - \frac{1}{2}\}$, then $\left[\frac{2x}{s} - \left(\left\lfloor \frac{x}{s} \right\rfloor + \left\lfloor \frac{x}{s} \right\rfloor\right)\right] > 0$ and $\left[\left\lfloor \frac{x}{s} \right\rfloor - \left\lfloor \frac{x}{s} \right\rfloor\right] > 0$. Thus, $\# > 0$.
2. If $x < 0$ and $\frac{x}{s} \notin \{\mathbb{Z}, \mathbb{Z} - \frac{1}{2}\}$, then $\left[\frac{2x}{s} - \left(\left\lfloor \frac{x}{s} \right\rfloor + \left\lfloor \frac{x}{s} \right\rfloor\right)\right] < 0$ and $\left[\left\lfloor \frac{x}{s} \right\rfloor - \left\lfloor \frac{x}{s} \right\rfloor\right] < 0$. Thus, $\# > 0$.
3. $\frac{x}{s} \in \{\mathbb{Z}, \mathbb{Z} - \frac{1}{2}\}$, then $\left[\frac{2x}{s} - \left(\left\lfloor \frac{x}{s} \right\rfloor + \left\lfloor \frac{x}{s} \right\rfloor\right)\right] = 0$ and $\left[\left\lfloor \frac{x}{s} \right\rfloor - \left\lfloor \frac{x}{s} \right\rfloor\right] > 0$. Thus, $\# = 0$.

Therefore, if $x \in \{\mathbb{Z}, \mathbb{Z} - \frac{1}{2}\}$, $\# = 0$. Otherwise, $\# > 0$. Plus, $P(x) > 0$. We can get

$$\begin{aligned}
 E(Err^f) - E(Err^r) &> 0 \\
 E(Err^f) &> E(Err^r)
 \end{aligned} \tag{A.4}$$

In conclusion, the flooring quantization would incur higher quantization error than the rounding quantization.

A.2.2. Complete deduction of Proof 1

We first recall **Proof 1**:

Proof 1 Given $b' < b$ and $x_q^r = s \cdot clip(\frac{x}{s}, 0, 2^{b'} - 1)$, we obtain $x_q^r = x_q - \lambda$, where $\lambda = s[clip(\frac{x}{s}, 2^{b'} - 1, 2^b - 1) - (2^{b'} - 1)]$. Thus, $Err^r = (x - x_q + \lambda)^2$. And, the possibility of $P(Err^r > Err)$ equates to $P(\lambda > 0)$.

To prove $P(Err' > Err)$ equates to $P(\lambda > 0)$, we first discuss when $Err' > Err$. We get

$$\begin{aligned}
 Err' - Err &= (x - x_q)^2 + 2\lambda(x - x_q) + \lambda^2 - (x - x_q)^2 \\
 &= 2\lambda(x - x_q) + \lambda^2 \\
 &= \lambda(2x - 2x_q + \lambda) \\
 &= \lambda(2x - x_q - (x_q - \lambda)) \\
 &= \lambda(2x - x_q - x'_q)
 \end{aligned} \tag{A.5}$$

We further discuss

1. If $\frac{x}{s} \leq 2^{b'} - 1$, then $\lambda = 0$. Thus, $Err' - Err = 0$.
2. If $\frac{x}{s} = 2^{b'} - \frac{1}{2}$, then $x'_q = s(2^{b'} - 1)$ and $x_q = s \cdot 2^{b'}$. Thus, $(2x - x_q - x'_q) = 0$. And, $Err' - Err = 0$.
3. If $\frac{x}{s} > 2^{b'} - 1$ and $\frac{x}{s} \neq 2^{b'} - \frac{1}{2}$, then $x'_q = s(2^{b'} - 1)$ and $\lambda > 0$. Thus,
 - (a) If $2^{b'} - 1 < \frac{x}{s} < 2^{b'} - \frac{1}{2}$, then $x'_q = x_q = 2^{b'} - 1 < x$. Therefore, $(2x - x_q - x'_q) > 0$.
 - (b) If $2^{b'} - \frac{1}{2} < \frac{x}{s} \leq 2^{b'}$, then $x - s(2^{b'} - 1) > s \cdot 2^{b'} - x$. Therefore, $x - x'_q > x_q - x \Rightarrow (2x - x_q - x'_q) > 0$.
 - (c) If $2^{b'} < \frac{x}{s}$, then $x - s(2^{b'} - 1) > s > \cdot 2^{b'} - x$. Therefore, $(2x - x_q - x'_q) > 0$.

In anyway, $(2x - x_q - x'_q) > 0$ and $\lambda > 0$. Thus, $Err' - Err > 0$.

In all, if $\lambda > 0$ and $\frac{x}{s} \neq 2^{b'} - \frac{1}{2}$, $Err' - Err > 0$. Otherwise, $Err' - Err = 0$. To simplify the equation and make the lower bound calculation, i.e. **Lemma 1**, easier, we can statistically approximate that $P(Err' > Err)$ equates to $P(\lambda > 0)$. The corresponding approximation loss is statistically negligible as well.

A.2.3. Theorem 1 in the bidirectional domain

Since we have already proven **Theorem 1** when $x \sim 2N(0, \sigma^2)|x > 0$ in the main text. Proving **Theorem 1** is still tenable in the bidirectional domain, i.e. $x \sim N(0, \sigma)$, is similar and easy.

First, we discuss when $x \sim N(0, \sigma^2)|x > 0$. With the exact same deduction process of **Proof 1**, we get "the quantization error would increase by the possibility of $P(x > \frac{2^{b'}-1}{2^{b-1}} \cdot 3\sigma|(x \sim N(0, \sigma^2), x > 0)$ ".

Second, we discuss when $x \sim N(0, \sigma^2)|x < 0$. Same to the above, we get "the quantization error would increase by the possibility of $P(x < -\frac{2^{b'}-1}{2^{b-1}} \cdot 3\sigma|(x \sim N(0, \sigma^2), x < 0)$ ".

Since $x \sim N(0, \sigma^2)$, $P(x < -\frac{2^{b'}-1}{2^{b-1}} \cdot 3\sigma|(x \sim N(0, \sigma^2), x < 0)$ would equate to $P(x > \frac{2^{b'}-1}{2^{b-1}} \cdot 3\sigma|(x \sim N(0, \sigma^2), x > 0)$.

Thus, for $x \sim N(0, \sigma^2)$, we get "the quantization error would increase by the possibility of $P(x > \frac{2^{b'}-1}{2^{b-1}} \cdot 3\sigma|(x \sim 2N(0, \sigma^2), x > 0)$ ". **Theorem 1** holds. So does **Lemma 1**.

A.3. Gradient calculations of $V_{th,l}^1$ and S_q^l

We adopt the same gradient calculations of the quantization step size of [13].

For $V_{th,l}^1$,

$$\begin{aligned}
 \frac{\partial L_{task}}{\partial V_{th,l}^1} &= \sum_t \sum_j \frac{1}{V_{th,l}^1} \frac{\partial L_{task}}{\partial S_{out,l}^t} \cdot g_{s,scale} \cdot g_q, \tag{A.6} \\
 g_q &= \begin{cases} \left[\frac{v_l^t}{V_{th,l}^1} + V_{th,l}^2 \right] - \frac{v_l^t}{V_{th,l}^1}, \frac{v_l^t}{V_{th,l}^1} \in [q_{min}, q_{max}] \\ 0, \frac{v_l^t}{V_{th,l}^1} < q_{min} \\ q_{max}, q_{max} < \frac{v_l^t}{V_{th,l}^1}, \end{cases} \tag{A.7}
 \end{aligned}$$

where the minimum quantization integer $q_{min} = 0$ and the maximum integer $q_{max} = 2^{B_{s,l}} - 1$. While, $g_{s,scale}$, equal to $\frac{1}{\sqrt{\sum_j 1 \cdot q_{max}}}$ and meant to avoid gradient explosion [13], is the gradient scaling factor. L_{task} represents the task loss signal.

For S_q^l ,

$$\begin{aligned}
 \frac{\partial L_{task}}{\partial S_q^l} &= \sum_i \frac{\partial L_{task}}{\partial w_q^l} \cdot g_{w,scale} \cdot g_q, \tag{A.8} \\
 g_q &= \begin{cases} \left[\frac{w_l}{S_q^l} \right] - \frac{w_l}{S_q^l}, \frac{w_l}{S_q^l} \in [q_{min}, q_{max}] \text{ and } B_{w,l} > 1 \\ \text{sign}(\frac{w_l}{S_q^l}) - \frac{w_l}{S_q^l}, \frac{w_l}{S_q^l} \in [q_{min}, q_{max}] \text{ and } B_{w,l} = 1 \\ q_{min}, \frac{w_l}{S_q^l} < q_{min} \\ q_{max}, q_{max} < \frac{w_l}{S_q^l}. \end{cases} \tag{A.9}
 \end{aligned}$$

Specially, when $B_{w,l} = 1$, $q_{min} = -1$ and $q_{max} = 1$. Otherwise, $q_{min} = -2^{B_{w,l}-1} + 1$ and $q_{max} = 2^{B_{w,l}-1} - 1$. Similarly, i is the index of the weight element, and $g_{w,scale} = \frac{1}{\sqrt{\sum_i 1 \cdot q_{max}}}$.

A.4. Gradient calculations of $B_{s,l}$ and $V_{th,l}^1$ of the bidirectional neuron

Since Equation 16 has a slightly different formulation, the corresponding gradient calculations of $B_{s,l}$ and $V_{th,l}^1$ would also change a bit.

For $B_{s,j}$,

$$\begin{aligned}
 \frac{\partial L_{task}}{\partial B_{s,l}} &= \frac{\partial L_{task}}{\partial B_{s,l}} = \sum_j \frac{\partial L_{task}}{\partial S_{put,l}^j} \cdot g_{s,scale} \cdot g_q, \tag{A.10} \\
 g_q &= \begin{cases} \text{sign}(\frac{v_l^t}{V_{th,l}^1}) \cdot (q_{max} + 1) \cdot \ln 2, \frac{v_l^t}{V_{th,l}^1} \notin [q_{min}, q_{max}] \\ 0, \text{otherwise.} \end{cases} \tag{A.11}
 \end{aligned}$$

Here, j is the index of the weight element, and $g_{s,scale} = \frac{1}{\sqrt{\sum_j 1 \cdot q_{max}}}$. Specially, when $B_{s,l} = 1$, $q_{min} = -1$ and $q_{max} = 1$. Otherwise, $q_{min} = -2^{B_{s,l}-1} + 1$ and $q_{max} = 2^{B_{s,l}-1} - 1$.

For $V_{th,l}^1$,

$$\frac{\partial L_{task}}{\partial V_{th,l}^1} = \sum_j \frac{\partial L_{task}}{\partial S_{out,l}^t} \cdot g_{s, scale} \cdot g_q, \quad (\text{A.12})$$

$$g_q = \begin{cases} \left\lfloor \frac{v_l^t}{V_{th,l}^1} \right\rfloor - \frac{v_l^t}{V_{th,l}^1}, \frac{v_l^t}{V_{th,l}^1} \in [q_{min}, q_{max}] \text{ and } B_{s,l} > 1 \\ \text{sign}\left(\frac{v_l^t}{V_{th,l}^1}\right) - \frac{v_l^t}{V_{th,l}^1}, \frac{v_l^t}{V_{th,l}^1} \in [q_{min}, q_{max}] \text{ and } B_{s,l} = 1 \\ q_{min}, \frac{v_l^t}{V_{th,l}^1} < q_{min} \\ q_{max}, q_{max} < \frac{v_l^t}{V_{th,l}^1}. \end{cases} \quad (\text{A.13})$$

Here, j is the index of the feature map element, $q_{min} = -2^{B_{s,l}-1} + 1$, and $q_{max} = 2^{B_{s,l}-1} - 1$. $g_{scale} = \frac{1}{\sqrt{\sum_j 1 \cdot q_{max}}}$.

A.5. Details of the experimental settings

All our experiments are conducted on A100 GPUs.

A.5.1. CIFAR

In the CIFAR experiments, two models are adopted ResNet20 and Spikformer. For ResNet20, we adhere to the default settings of [18] and [19]. The training epochs are set to 200, batch size to 128, and learning rate to 0.1. Besides, the penalty coefficients λ_1 , λ_2 , and λ_3 are set to $4e-2$, $4e-2$, and $1e-2$, respectively. The initial W/S/T are set to 4/4/2. These settings apply to both comparative and ablation studies. For Spikformer, we adopt the same default settings as [56] from their official codes, including every training configuration. The penalty coefficients and the initial W/S/T are the same as our ResNet setting.

Additionally, $B_{w,bound}$, $B_{s,bound}$, and T_{bound} are set to 6, 6, and 3, respectively.

A.5.2. ImageNet

In the ImageNet-1k experiments, we exclusively adopt the SEWResNet34 model. The training codes are also built on the default [18]. The training epochs are set to 200, batch size to 128×4 (data distributed parallel on 4 GPU cards), and learning rate to 0.1. Besides, the penalty coefficients λ_1 , λ_2 , and λ_3 are set to $8e-2$, $8e-2$, and $1e-2$, respectively. Following those advanced SNNs, e.g., [39] and [52], we directly set time-step=1 to demonstrate our model's superior accuracy on large-scaled ImageNet, i.e., the initial W/S/T are set to 4/4/1. In Section A.7, we also show the result of the initial W/S/T=4/4/2.

Additionally, $B_{w,bound}$, $B_{s,bound}$, and T_{bound} are set to 6, 6, and 2, respectively.

A.5.3. CIFAR10-DVS

In the CIFAR10-DVS experiments, we only use the default DVS Spikformer defined by the official codes of [56]. To better observe the temporal dimension's influence on the model accuracy of the event dataset. We set T_l back to the unlearnable constant and the corresponding temporal

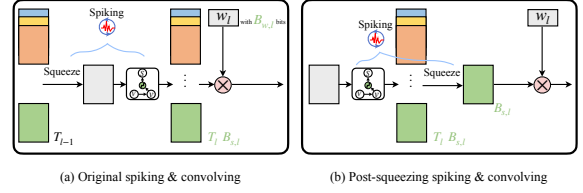


Figure A.1: Different computation pipelines with the temporal squeezing. **(a)** the conventional computing pipeline. The input current is squeezed before the spiking operation. **(b)** the identical post-squeezing pipeline. The temporal squeezing operation is conducted after the spiking operation.

squeezing is also deactivated. The corresponding penalty coefficients λ_1 and λ_3 are all set to $4e-2$. The target weight bit widths are all set to 1, the target spike bit widths are 2 or 4. Under this setting, SNNs can fully exploit the model-level sequential processing ability. Thus, we can accurately observe that our methods can mitigate "the temporal constraint" steadily. In Section A.7, we also list the results of applying the learnable temporal lengths and temporal squeezing.

Additionally, $B_{w,bound}$ and $B_{s,bound}$ are both set to 6. And, W/S are initial to 4/4. For experiments with learnable T_l in Table A.2, we cancel the temporal-wise sharing and reset λ_1 to $8e-2$.

A.5.4. DVS-GESTURE

In the DVS-GESTURE experiments, we also use the default DVS Spikformer defined by the official codes of [56]. Most experimental settings are the same as the CIFAR10-DVS experiments and the official codes [56]. Following is some exceptions: the training epoch is set to 192, and when the target time length is 1, 2, or x ($x > 2$), each event data is divided into 4, 10, or 16 temporal slices, respectively. Only the first 1, 2, or x temporal slices are extracted to training and inference.

A.5.5. Additional statements about the quantization baselines

The closest baseline-work to ours is [39]. However, we find that their work is not open-sourced and lacks a lot of implementation details. Therefore, we try to reproduce their method based on their paper and our practice as we call "U-quant." in the main text. Nevertheless, we also find many of their statistics, such as S-ACE, may be roughly calculated so we have to re-calculate every statistics we show in the main text with more accurate means.

In addition, we also stop citing some of their results that we fail reproducing, and report the "U-quant." results instead.

A.6. Elaborations on how temporal squeezing would save S-ACE

Our proposed temporal squeezing uses the mean operation to extract the temporal information.

One merit of using the mean operation is the squeezed data will not require any extra bit width. For instance, for

a positive spike train $S_{out} = \{S_{out}^1, S_{out}^2, \dots, S_{out}^t, \dots, S_{out}^T\}$. Each spike S_{out}^t has B_s bits. To contain the squeezed spike map $\hat{S}_{out} = \frac{1}{T} \sum_{t=1}^T S_{out}^t$ without any loss, B_s bits would be enough. This gives us the opportunity to reduce the S-ACE of SNNs' convolution by changing the computing pipeline.

As shown in Figure A.1, the conventional spiking-and-convolving pipeline will require $T_l \times B_s \times B_w \times MAC$ S-ACEs. With the changed post-squeezing pipeline, we only need $B_s \times B_w \times MAC$ S-ACEs to implement the identical computation. Thus, when the overall T_l 's of SNNs are over 2, such computation advantage of the temporal squeezing would be more pronounced.

A.7. Additional experimental results on ImageNet and CIFAR10-DVS

In this section, we add more experimental results as expanded evidence to validate more aspects of our methods.

Firstly, as described in Section A.5, we use the initial $T=1$ in the main text. This may raise the concern about whether the temporal squeezing cannot function well on such up-scaled dataset. As shown in Table A.1, with the temporal squeezing, the model can achieve the same model accuracy while using fewer S-ACEs, handling the change of temporal length from 2 to 1 during training well. As for the reason why the model initialized as $W/S/T=4/4/2$ can perform better on accuracy very slightly. One explanation is that the initial temporal length does not affect the model performance while the target temporal length (or the actual temporal length) does, which is in line with the prior finding of [39] that the temporal length rarely affects the performance of multi-bit SNNs on static datasets. Therefore, for the saving of training time, we choose to set the initial temporal length as 1 in the experiments of the main text since the longer initial temporal length causes longer forward and backward inference time. Additionally, from another perspective, this could further prove that our multi-bit SNN has advanced its spatial processing ability to the limit, one time-step would suffice to fulfill the requirement of a high-accuracy inference.

In addition, we also naively apply our methods to Spikformer-8-512 on ImageNet with the same model hyperparameters as [39] and [56]. Their models achieve 70.87% [39] and 73.38% [56] with $W/S/T = 4/2/1$ and $16/1/4$, respectively. While, our Spikformer achieves a higher 74.87% top-1 accuracy with lower bit budgets that $W/S/T = 2.64/2.21/1.0$.

Table A.1
Additional experimental results on ImageNet.

Method	Architecture	W/S/T	Bit Budget	S-ACE	Top-1
Attention-SNN	ResNet34	16/1/1	16	56.73	69.15
TET	Sew-ResNet34	16/1/4	64	226.93	68.00
Ternary Spike	ResNet34	16/2/4	128	435.86	70.74
PLIF+SEW	SEW-ResNet34	16/1/4	64	226.93	67.04
	SEW-ResNet50	16/1/4	64	215.62	67.78
Quant. SNN	SEW-ResNet34	8/8/1	64	226.93	70.13
Ours-441-221		2.58/2.18/1.0	5.61	30.74	70.57
Ours-441-241	SEW-ResNet34	2.62/3.96/1.0	10.39	54.69	72.02
Ours-442-241		2.60/4.01/1.0	10.41	54.26	72.11

"Ours-xxx-yyy" denotes the initial $W/S/T=x/y/z$ and the target $W/S/T=y/z/y$.

Secondly, as stated in Section A.5, we use the conventional sequential-processing pipeline to address the event dataset in the main text, i.e., the temporal squeezing and learnable T are canceled. In this way, we can accurately control the temporal length and fully utilize the model-level temporal processing of SNN. This may raise the concern that the temporal squeezing could severely impair the temporal processing ability. As shown in Table A.2, we find the temporal squeezing can still outperform the quantization baseline [39] and maintain good performance under low time-steps, although the overall model performance, compared to the case without temporal squeezing, is decreased. One possible explanation is that although the model-level temporal processing ability may be diminished, the layer-wise temporal processing ability can still be maintained when using temporal squeezing. And, temporal squeezing also meets the temporal information dynamics that as the training goes on, more valuable and decisive information aggregates into the early time-steps [26]. As listed in Table A.2, the best results of temporal squeezing show up under the low time-step settings. Temporal squeezing merely accelerates the aggregation process. That is why temporal squeezing would not severely undermine the sequential-processing ability and perform well even on the sequential dataset.

Table A.2
Additional experimental results of Spikformer (Spf.) on CIFAR10-DVS.

W/S/T	Top-1	Origin[39]		Quant. Spf.[39]		Our Spf.		Our Spf. w/ Learnable T_l	
		W/S/T	Top-1	W/S/T	Top-1	W/S/T	Top-1	W/S/T	Top-1
16/1/16	80.7	1/1/16	79.8	1.11/2.00/6.0	80.9	1.14/1.97/6.00	78.7		
		1/2/8	79.3	1.28/2.00/4.0	80.0	1.14/1.97/4.00	79.3		
		1/4/4	63.1	1.33/4.00/3.0	80.1	1.17/4.08/2.05	79.6		
		1/8/2	43.0	1.31/4.03/2.0	78.7	1.09/1.95/1.95	80.0		
		1/16/1	35.8	1.31/4.03/1.0	77.4	1.11/1.49/1.00	77.3		

Additional statements on temporal squeezing. Although we have clarified the purpose of using temporal squeezing in the main text, we would like to highlight it here one more time. The idea of proposing temporal squeezing is tackling the interlayer data mismatching issue and deriving the gradient for T_l . Only in this way could the temporal bit widths be adaptively allocated throughout different layers and make dataflow smooth. Temporal squeezing is more of a technical resolution for applying the mixed-precision framework to SNNs. We do not expect this technique can bring any model performance advancement

Our main contributions are refining the spiking neuron, the formulation of the temporal-related step-size mismatch issue, and the step-size renewal mechanism. All of them are validated through various experiments as we showed in the main text.

A.8. Maintaining the asynchronous nature of SNNs

The most precious characteristic that SNN brings is its asynchronous processing ability, i.e., event-driven and clock-free computing. We would like to address the possible concerns about how such nature could be maintained when

temporal squeezing is applied and could there exist potential issues.

Exploiting the spike perceptrons. *Temporal squeezing itself is consistent with neurodynamics as it is essentially composed of a signal accumulation [17] and a division operation.* A similar accumulation mechanism can also be found in the current accumulation stage of spiking neuron, such as LIF and IF. Particularly, SpikeConverter neuron [32] separates this accumulation from the spiking neuron modeling and uses a particular computing pipeline to handle this accumulation. Their accumulation is identical to ours, which is proven feasible in asynchronous computing. In addition, such accumulation has also been realized and implemented by neuromorphic circuits to process the DVS signals and generate the dynamic datasets [2, 31].

As such, we can simply use the same signal accumulation diagrams, i.e. the spike perceptrons, to realize temporal squeezing as what has been used in DVS cameras [28] and previous spiking neurons [32]. In other words, such different computing paradigm as shown in Figure A.1 can be implemented under the existing neuromorphic computing and will not cause any loss of the asynchronous and clock-free nature.

Using the two-stage pipeline or keeping single time-step. Although we have theoretically elaborated on the harmlessness of temporal squeezing to the asynchronous nature in the above, one may argue that the entire network’s spike flow could be interrupted by the squeezing stage, leading to longer inference latency. This concern has already discussed and resolved by [32], using the two-stage pipeline. The first stage is spike accumulation, i.e., the temporal squeezing, the second stage is spike emission. These two separate stages can overlapped inter-layer. Specifically, assuming spike accumulation and emission both require 4 hardware clock cycles for computing. After the first cycle of the spike emission of the previous layer, the first computing cycle of the spike accumulation of the next layer can be started instead of waiting for the whole 4 cycles of the spike emission of the previous layer being finished. Thus, 3 cycles are overlapped, and the actual latency of the two-stage spiking pipeline is only 5 cycles, only one more cycle that the ordinary spiking pipeline. Therefore, using temporal squeezing only introduces very limited latency increase.

Such concern can also be resolved by the fact that we only use one or two time-steps to achieve the most advanced model accuracy on static datasets as shown in the main text. As for the event dataset, we have also mitigated the temporal constraint. High accuracy can be maintained for the event data, even when the temporal lengths are extremely short. Therefore, the model-level asynchronous dataflow can be well maintained in our framework without drastically longer-latency issue.

Canceling temporal squeezing. Even in the worst-case assumption that temporal squeezing had no neuromorphic hardware support and must be applied to the long temporal length, we could simply cancel this mechanism and give up the learnable T_l as the solution because as we have stated

before: temporal squeezing is more of a technical resolution for applying the mixed-precision framework to SNNs. Moreover, our main contributions are refining the spiking neuron, the formulation of the temporally related step-size mismatch issue, and the step-size renewal mechanism. As the experiments of Table A.2 on the event dataset show our methods can achieve better model performance without temporal squeezing, and temporal squeezing, aiming at realizing learnable and layer-wise different T_l , will not undermine the temporal-processing ability of SNNs as well.

A.9. Overall algorithm of the proposed bit allocation

For clarity, we provide the pseudo code of the overall algorithm, as shown in Algorithm A.1.

Algorithm A.1 Overall training pipeline of the proposed adaptive-bit-allocation SNNs.

Input: Target W/S/T B_w^{tar} , B_s^{tar} , and T^{tar} ; penalty coefficients λ_1 , λ_2 , and λ_3 ; full-precision SNN with our refined spiking neurons, L layers, and weights w_l ; the actual bit widths of each layer $B_{s,l}^t$, $B_{w,l}$, and T_l ; the corresponding quantization step sizes $V_{th,l}^{1,t}$ and S_q^l ; the training dataset D ; the training epochs ep ; the training batch size bs .

Output: mixed-precision SNN.

- 1: Initialize the bit-width observers in Algorithm 1.
- 2: Initialize $V_{th,l}^{1,t}$ and S_q^l using the first mini-batch of D .
- 3: The shutting thresholds $Th_w \leftarrow 0.24|\bar{B}_{w,l} - B_w^{tar}|$ and $Th_s \leftarrow 0.24|\bar{B}_{s,l}^t - B_s^{tar}|$.
- 4: Renewal flags $f_w \leftarrow 0$ and $f_s \leftarrow 0$
- 5: for $i = 1; i \leq ep; i++$ do
- 6: for $j = 1; j \leq \text{ceil}(\frac{D}{bs}); j++$ do
- 7: for $l = 1; l \leq L; l++$ do
- 8: # the step-size renewal of weight
- 9: if $|\bar{B}_w - B_w^{tar}| > Th_w$ and $f_w == 0$ do
- 10: $S_q^l \leftarrow \text{RA}(B_{w,l}, w_l)$
- 11: else do
- 12: $f_w \leftarrow 1$
- 13: # the step-size renewal of spike activation
- 14: if $|\bar{B}_s - B_s^{tar}| > Th_s$ and $f_s == 0$ do
- 15: $V_{th,l}^{1,t} \leftarrow \text{RA}(B_{s,l}^t, v_l^t)$
- 16: else do
- 17: $f_s \leftarrow 1$
- 18: $S_{out,l} \leftarrow \text{SNN}_l(S_{out,l-1}, V_{th,l}^{1,t}, w_l, S_q^l)$
- 19: $L_{total} \leftarrow L_{task} + \lambda_1 L(\bar{B}_w, B_w^{tar}) + \lambda_2 L(\bar{T}, T^{tar}) + \lambda_3 L(\bar{B}_s, B_s^{tar})$
- 20: Back-propagation and updating SNN parameters

RA denotes the renewal algorithm (Algorithm 1). \bar{x} denotes the averaged value of x over the whole net.

CRedit authorship contribution statement

Yao Xingting: Writing – original draft, Writing – review & editing, Conceptualization, Investigation, Data curation, Formal analysis, Software, Project administration, Resources. **Hu Qinghao:** Writing – review & editing, Methodology, Formal analysis, Supervision. **Zhou Fei:** Writing – review & editing, Funding acquisition. **Liu Tielong:** Writing – review & editing, Formal analysis. **Li Gang:** Writing – review & editing. **Wang Peisong:** Writing – review & editing. **Cheng Jian:** Writing – review & editing, Funding acquisition.

References

- [1] Akopyan, F., Sawada, J., Cassidy, A., Alvarez-Icaza, R., Arthur, J., Merolla, P., Imam, N., Nakamura, Y., Datta, P., Nam, G.J., et al., 2015. Truenorth: Design and tool flow of a 65 mw 1 million neuron programmable neurosynaptic chip. *IEEE transactions on computer-aided design of integrated circuits and systems* 34, 1537–1557.
- [2] Amir, A., Taba, B., Berg, D., Melano, T., McKinstry, J., Di Nolfo, C., Nayak, T., Andreopoulos, A., Garreau, G., Mendoza, M., et al., 2017. A low power, fully event-based gesture recognition system, in: *Proceedings of the IEEE conference on computer vision and pattern recognition*, pp. 7243–7252.
- [3] Bengio, Y., Léonard, N., Courville, A., 2013. Estimating or propagating gradients through stochastic neurons for conditional computation. *arXiv preprint arXiv:1308.3432*.
- [4] Bittar, A., Garner, P.N., 2022. A surrogate gradient spiking baseline for speech command recognition. *Frontiers in Neuroscience* 16, 865897.
- [5] Bohte, S.M., Kok, J.N., La Poutré, J.A., 2000. Spikeprop: backpropagation for networks of spiking neurons., in: *ESANN, Bruges*. pp. 419–424.
- [6] Chen, W., Wang, P., Cheng, J., 2021. Towards mixed-precision quantization of neural networks via constrained optimization, in: *Proceedings of the IEEE/CVF International Conference on Computer Vision (ICCV)*, pp. 5350–5359.
- [7] Choi, J., Wang, Z., Venkataramani, S., Chuang, P.I.J., Srinivasan, V., Gopalakrishnan, K., 2018. Pact: Parameterized clipping activation for quantized neural networks. *arXiv preprint arXiv:1805.06085*.
- [8] Cramer, B., Stradmann, Y., Schemmel, J., Zenke, F., 2020. The heidelberg spiking data sets for the systematic evaluation of spiking neural networks. *IEEE Transactions on Neural Networks and Learning Systems* 33, 2744–2757.
- [9] Deng, J., Dong, W., Socher, R., Li, L.J., Li, K., Fei-Fei, L., 2009. Imagenet: A large-scale hierarchical image database, in: *2009 IEEE conference on computer vision and pattern recognition, Ieee*. pp. 248–255.
- [10] Deng, L., Wu, Y., Hu, X., Liang, L., Ding, Y., Li, G., Zhao, G., Li, P., Xie, Y., 2020. Rethinking the performance comparison between snns and anns. *Neural networks* 121, 294–307.
- [11] Deng, S., Li, Y., Zhang, S., Gu, S., 2021. Temporal efficient training of spiking neural network via gradient re-weighting, in: *International Conference on Learning Representations*.
- [12] Dong, Z., Yao, Z., Gholami, A., Mahoney, M.W., Keutzer, K., 2019. Hawq: Hessian aware quantization of neural networks with mixed-precision, in: *Proceedings of the IEEE/CVF international conference on computer vision*, pp. 293–302.
- [13] Esser, S.K., McKinstry, J.L., Bablani, D., Appuswamy, R., Modha, D.S., 2020. Learned step size quantization, in: *International Conference on Learning Representations*.
- [14] Fang, W., Chen, Y., Ding, J., Yu, Z., Masquelier, T., Chen, D., Huang, L., Zhou, H., Li, G., Tian, Y., 2023. Spikingjelly: An open-source machine learning infrastructure platform for spike-based intelligence. *Science Advances* 9, eadi1480.
- [15] Fang, W., Yu, Z., Chen, Y., Huang, T., Masquelier, T., Tian, Y., 2021. Deep residual learning in spiking neural networks. *Advances in Neural Information Processing Systems* 34.
- [16] Feng, L., Liu, Q., Tang, H., Ma, D., Pan, G., . Multi-level firing with spiking ds-resnet: Enabling better and deeper directly-trained spiking neural networks .
- [17] Gerstner, W., Kistler, W.M., Naud, R., Paninski, L., 2014. *Neuronal dynamics: From single neurons to networks and models of cognition*. Cambridge University Press.
- [18] Guo, Y., Chen, Y., Liu, X., Peng, W., Zhang, Y., Huang, X., Ma, Z., 2024. Ternary spike: Learning ternary spikes for spiking neural networks, in: *Proceedings of the AAAI Conference on Artificial Intelligence*, pp. 12244–12252.
- [19] Guo, Y., Zhang, L., Chen, Y., Tong, X., Liu, X., Wang, Y., Huang, X., Ma, Z., 2022. Real spike: Learning real-valued spikes for spiking neural networks, in: *European Conference on Computer Vision*, Springer. pp. 52–68.
- [20] Hammouamri, I., Khalfaoui-Hassani, I., Masquelier, T., 2023. Learning delays in spiking neural networks using dilated convolutions with learnable spacings. *arXiv preprint arXiv:2306.17670*.
- [21] He, W., Wu, Y., Deng, L., Li, G., Wang, H., Tian, Y., Ding, W., Wang, W., Xie, Y., 2020. Comparing snns and rnns on neuromorphic vision datasets: Similarities and differences. *Neural Networks* 132, 108–120.
- [22] Hu, Y., Deng, L., Wu, Y., Yao, M., Li, G., 2024. Advancing spiking neural networks toward deep residual learning. *IEEE Transactions on Neural Networks and Learning Systems*.
- [23] Hu, Y., Tang, H., Pan, G., 2021. Spiking deep residual networks. *IEEE Transactions on Neural Networks and Learning Systems* 34, 5200–5205.
- [24] Huang, X., Shen, Z., Li, S., Liu, Z., Xianghong, H., Wicaksana, J., Xing, E., Cheng, K.T., 2022. Sdq: Stochastic differentiable quantization with mixed precision, in: *International Conference on Machine Learning, PMLR*. pp. 9295–9309.
- [25] Kim, H.B., Lee, J.H., Yoo, S., Kim, H.S., 2024. Metamix: Meta-state precision searcher for mixed-precision activation quantization, in: *Proceedings of the AAAI Conference on Artificial Intelligence*, pp. 13132–13141.
- [26] Kim, Y., Li, Y., Park, H., Venkatesha, Y., Hambitzer, A., Panda, P., 2023. Exploring temporal information dynamics in spiking neural networks. *Proceedings of the AAAI Conference on Artificial Intelligence* 37, 8308–8316. URL: <https://ojs.aaai.org/index.php/AAAI/article/view/26002>, doi:10.1609/aaai.v37i17.26002.
- [27] Krizhevsky, A., Hinton, G., et al., 2009. Learning multiple layers of features from tiny images .
- [28] Li, H., Liu, H., Ji, X., Li, G., Shi, L., 2017. Cifar10-dvs: an event-stream dataset for object classification. *Frontiers in neuroscience* 11, 309.
- [29] Li, Y., Guo, Y., Zhang, S., Deng, S., Hai, Y., Gu, S., 2021. Differentiable spike: Rethinking gradient-descent for training spiking neural networks. *Advances in Neural Information Processing Systems* 34.
- [30] Li, Y., Zeng, Y., . Efficient and accurate conversion of spiking neural network with burst spikes .
- [31] Lin, Y., Ding, W., Qiang, S., Deng, L., Li, G., 2021. Es-imagenet: A million event-stream classification dataset for spiking neural networks. *Frontiers in neuroscience* 15, 726582.
- [32] Liu, F., Zhao, W., Chen, Y., Wang, Z., Jiang, L., 2022. Spikeconverter: An efficient conversion framework zipping the gap between artificial neural networks and spiking neural networks, in: *Proceedings of the AAAI Conference on Artificial Intelligence*, pp. 1692–1701.
- [33] Maass, W., 1997. Networks of spiking neurons: the third generation of neural network models. *Neural networks* 10, 1659–1671.
- [34] Mao, R., Tang, L., Yuan, X., Liu, Y., Zhou, J., 2024. Stellar: Energy-efficient and low-latency snn algorithm and hardware co-design with spatiotemporal computation, in: *2024 IEEE International Symposium on High-Performance Computer Architecture (HPCA)*, IEEE. pp. 172–185.
- [35] Meng, Q., Xiao, M., Yan, S., Wang, Y., Lin, Z., Luo, Z.Q., 2022. Training high-performance low-latency spiking neural networks

- by differentiation on spike representation, in: Proceedings of the IEEE/CVF conference on computer vision and pattern recognition, pp. 12444–12453.
- [36] Rath, N., Srinivasan, G., Panda, P., Roy, K., 2020. Enabling deep spiking neural networks with hybrid conversion and spike timing dependent backpropagation. arXiv preprint arXiv:2005.01807 .
- [37] Rumelhart, D.E., Hinton, G.E., Williams, R.J., 1986. Learning representations by back-propagating errors. *nature* 323, 533–536.
- [38] Sengupta, A., Ye, Y., Wang, R., Liu, C., Roy, K., 2019. Going deeper in spiking neural networks: Vgg and residual architectures. *Frontiers in neuroscience* 13, 95.
- [39] Shen, G., Zhao, D., Li, T., Li, J., Zeng, Y., 2024. Are conventional snns really efficient? a perspective from network quantization, in: Proceedings of the IEEE/CVF Conference on Computer Vision and Pattern Recognition, pp. 27538–27547.
- [40] Sun, P., Chua, Y., Devos, P., Botteldooren, D., 2023. Learnable axonal delay in spiking neural networks improves spoken word recognition. *Frontiers in Neuroscience* 17, 1275944.
- [41] Sun, P., Wu, J., Zhang, M., Devos, P., Botteldooren, D., 2024. Delayed memory unit: modeling temporal dependency through delay gate. *IEEE transactions on neural networks and learning systems* .
- [42] Uhlich, S., Mauch, L., Cardinaux, F., Yoshiyama, K., Garcia, J.A., Tiedemann, S., Kemp, T., Nakamura, A., 2019. Mixed precision dnns: All you need is a good parametrization. arXiv preprint arXiv:1905.11452 .
- [43] Wang, K., Liu, Z., Lin, Y., Lin, J., Han, S., 2019. Haq: Hardware-aware automated quantization with mixed precision, in: Proceedings of the IEEE/CVF conference on computer vision and pattern recognition, pp. 8612–8620.
- [44] Wu, B., Wang, Y., Zhang, P., Tian, Y., Vajda, P., Keutzer, K., 2018a. Mixed precision quantization of convnets via differentiable neural architecture search. arXiv preprint arXiv:1812.00090 .
- [45] Wu, Y., Deng, L., Li, G., Zhu, J., Shi, L., 2018b. Spatio-temporal backpropagation for training high-performance spiking neural networks. *Frontiers in neuroscience* 12, 331.
- [46] Wu, Y., Deng, L., Li, G., Zhu, J., Xie, Y., Shi, L., 2019. Direct training for spiking neural networks: Faster, larger, better, in: Proceedings of the AAAI Conference on Artificial Intelligence, pp. 1311–1318.
- [47] Wu, Z., Zhang, H., Lin, Y., Li, G., Wang, M., Tang, Y., 2021. Liaf-net: Leaky integrate and analog fire network for lightweight and efficient spatiotemporal information processing. *IEEE Transactions on Neural Networks and Learning Systems* .
- [48] Xiao, Y., Tian, X., Ding, Y., Ding, P., Jing, M., Zuo, L., 2024. Multi-bit mechanism: A novel information transmission paradigm for spiking neural networks. arxiv preprint arxiv:2407.05739 .
- [49] Xing, X., Gao, B., Zhang, Z., Clifton, D.A., Xiao, S., Du, L., Li, G., Zhang, J., 2024a. Spikellm: Scaling up spiking neural network to large language models via saliency-based spiking. arXiv preprint arXiv:2407.04752 .
- [50] Xing, X., Zhang, Z., Ni, Z., Xiao, S., Ju, Y., Fan, S., Wang, Y., Zhang, J., Li, G., 2024b. Spikelm: Towards general spike-driven language modeling via elastic bi-spiking mechanisms. arXiv preprint arXiv:2406.03287 .
- [51] Yao, M., Gao, H., Zhao, G., Wang, D., Lin, Y., Yang, Z., Li, G., 2021. Temporal-wise attention spiking neural networks for event streams classification, in: Proceedings of the IEEE/CVF International Conference on Computer Vision, pp. 10221–10230.
- [52] Yao, M., Zhao, G., Zhang, H., Hu, Y., Deng, L., Tian, Y., Xu, B., Li, G., 2023. Attention spiking neural networks. *IEEE transactions on pattern analysis and machine intelligence* .
- [53] Yao, X., Li, F., Mo, Z., Cheng, J., 2022. Glif: A unified gated leaky integrate-and-fire neuron for spiking neural networks. *Advances in Neural Information Processing Systems* 35, 32160–32171.
- [54] Zhang, Z., Shao, W., Gu, J., Wang, X., Luo, P., 2021. Differentiable dynamic quantization with mixed precision and adaptive resolution, in: International Conference on Machine Learning, PMLR. pp. 12546–12556.
- [55] Zheng, H., Wu, Y., Deng, L., Hu, Y., Li, G., 2021. Going deeper with directly-trained larger spiking neural networks, in: Proceedings of the AAAI Conference on Artificial Intelligence, pp. 11062–11070.
- [56] Zhou, Z., Zhu, Y., He, C., Wang, Y., Yan, S., Tian, Y., Yuan, L., 2022. Spikformer: When spiking neural network meets transformer. arXiv preprint arXiv:2209.15425 .
- [57] Zhu, S., Dong, X., Su, H., 2019. Binary ensemble neural network: More bits per network or more networks per bit?, in: Proceedings of the IEEE/CVF conference on computer vision and pattern recognition, pp. 4923–4932.